

Detection of unexpected leading delays in broad $H\beta$ line reverberations in the quasar PHL 1092

Jian-Min Wang^{1,2,3}, Chen Hu¹, Yong-Jie Chen^{4,1,2}, Yu-Yang Songsheng¹, Yi-Lin Wang^{1,2}, Hao Zhang^{1,2}, Pu Du¹, Yan-Rong Li¹, Bin Luo^{5,6}, Michael S. Brotherton⁷, Jin-Ming Bai⁸, Wei-Jian Guo³, Seng Yang⁹, Zhu-Heng Yao³, Jesús Aceituno^{10,11}

¹*Key Laboratory for Particle Astrophysics, Institute of High Energy Physics, Chinese Academy of Sciences, 19B Yuquan Road, Beijing 100049, China*

²*School of Astronomy and Space Science, School of Physical Sciences, University of Chinese Academy of Sciences, 19A Yuquan Road, Beijing 100049, China*

³*National Astronomical Observatories of China, Chinese Academy of Sciences, 20A Datun Road, Beijing 100020, China*

⁴*Technology and Engineering Center for Space Utilization, Chinese Academy of Sciences, Beijing 100094, P. R. China*

⁵*School of Astronomy and Space Science, Nanjing University, Nanjing 210093, China*

⁶*Key Laboratory of Modern Astronomy and Astrophysics, Ministry of Education, China*

⁷*Department of Physics and Astronomy, University of Wyoming, Laramie, WY 82071, USA*

⁸*Yunnan Observatory, Chinese Academy of Sciences, Kunming 650011, China*

⁹*School of Physics and Electrical Engineering, Anyang Normal University, Anyang, Henan 455000, China*

¹⁰*Centro Astronomico Hispano Alemán, Sierra de los filabres sn, E-04550 Gergal, Almería, Spain*

¹¹*Instituto de Astrofísica de Andalucía, Glorieta de la astronomía sn, 18008 Granada, Spain*

Delayed reverberations of broad emission lines in response to optical continuum variations^{1,2} have been widely observed in active galactic nuclei (AGNs). They serve as a powerful tool for probing inner structures of AGNs^{3,4} and estimating the masses of supermassive black holes (SMBHs)⁵. The delays exhibit a strong correlation with approximately the square root of the optical luminosity – a relationship known as the "standard structure" of AGN broad-line regions (BLRs)^{3,4,6,7}. Here, we report the discovery of leading delays in $H\beta$ line re-

reverberations (LDRs) in the quasar PHL 1092 preceding variations of the 5100 Å continuum by 17–57 days, based on our eight-year continuous campaign of reverberation mapping of super-Eddington AGNs. The LDRs suggest that the 5100 Å continuum regions are so extensive that they are larger than the BLRs. This phenomenon not only fundamentally disrupts the well-established BLR size-luminosity relation but also violates the principle of causality. This unprecedented LDRs challenge the conventional methods for estimating SMBH mass as well as the standard model of AGNs. A preferred scenario to explain the LDRs is that the SMBH-disk contains a population of accreting stellar-mass black holes (sMBHs)^{8–10} as extra heating sources of the disk. Consequently, continuum regions of the disk are efficiently stretched so that the 5100 Å regions exceed the BLRs, yielding the observed LDRs. Generally, sMBH activities there could provide new physics of AGN phenomena, which can be tested by LIGO, LISA¹¹/Tianqin¹² and ET¹³ detections of gravitational waves from SMBH mergers.

With great efforts of measuring the H β lags ($\tau_{H\beta}$) relative to the 5100 Å continuum from reverberation mapping (RM) campaigns, a robust empirical relation of $R_{H\beta} \approx 33.6 \ell_{44}^{0.53}$ ltd has been established over more than four decades (see a brief summary in § 1 of Method), commonly referred to as the $R - L$ relation. Here $R_{H\beta} = c\tau_{H\beta}$ denotes the size of the broad-line region (BLR), c is the speed of light, and $\ell_{44} = L_{5100}/10^{44} \text{ erg s}^{-1}$ represents the 5100 Å luminosity normalized to $10^{44} \text{ erg s}^{-1}$. This relation serves as a benchmark of AGN structure widely applied to all kinds of quasars including large samples^{14,15} for cosmic black hole demography from $z \sim 7.5$ including the JWST quasars¹⁶ and little red dots (LRDs)¹⁷. However, the long-term SEAMBH (Super-Eddington Accreting Massive Black Holes) campaign^{18–20}, which is a program designed to investigate physics of super-Eddington AGNs, has found that $R_{H\beta}$ significantly shrinks with increases of the relative strength of optical iron lines to H β (\mathcal{R}_{Fe})⁷. One of the primary goals of this campaign has been searching for the mostly extreme shortening of H β lags in super-Eddington AGNs, where the intrinsic timescales $R_{H\beta}/c$ approach ones comparable to the light-crossing time of the SMBH-disk itself. If such an extreme object exists, what observational signatures would its reverberations

exhibit? and what underlying physics would they reveal?

PHL 1092 is one of the long-term targets selected as an extremely high- \mathcal{R}_{Fe} AGN^{21–23} (see recent reviews on observational properties of SEAMBHs as a function of \mathcal{R}_{Fe} ^{24,25}). Fig. 1 presents its optical spectra, multi-wavelength spectral energy distributions (SEDs), and an extreme position in the $\mathcal{R}_{\text{Fe}} - \text{FWHM}(\text{H}\beta)$ plane^{21,26}. Obviously, it is an AGN with a high Eddington ratio, and its SED is notably bluer than the average SED of quasars. Additionally, PHL 1092 is known as a weak-line quasar²⁷, and its X-ray emissions exhibit strong variability²². Our campaign of PHL 1092 has been conducted continuously since November 2017, spanning eight years. Details of observations and data reduction are described in § 2.

Tab. 1 provides the spectral features of PHL 1092 and additional relevant information. Fig. 1a displays the annually averaged spectra, showing roughly constant profiles of the $\text{H}\beta$ line over the past eight years. This indicates that the BLRs are relatively stable but with only flux variations shown in the light curves (LCs). Fig. 2 shows the LCs of PHL 1092 alongside the results of reverberation analysis. Despite all the challenges of determining lags from a single annual campaign, we remained steadfast in our pursuit from our long term campaigns year after year. Given the BLR fluctuations observed in this object, we conducted RM analysis across different epochs using the MICA and JAVELIN codes (see § 3), intentionally excluding phases characterized by non-concordant reverberations discussed in § 4. Tab. 2 provides flux variability (F_{var}), and delays, which are in good agreement with one another. We find that the $\text{H}\beta$ variations strongly correlate with the 5100 Å continuum, namely, $\text{H}\beta$ reverberations are indeed taking place, however, the $\text{H}\beta$ reverberations are preceding the varying continuum with the lead of $\tau_{\text{H}\beta}^{\ell} = -(17 \sim 57)$ days given in Tab. 2. We note that the damped random walk (DRW) model doesn't fit well at epochs around MJD-58000+800 and +2500 (in timescales of one half years or so much shorter than the entire campaign). These could may result from non-concordant reverberations of the BLR composite responses with respect to spatially inhomogeneous variations of the extended ionizing sources.

See § 4 for a toy model that discuss the non-concordant reverberations of the ideal cases.

Based on the spectral features, we derived H β lags of $\tau_{\text{H}\beta}^0 = (128.7, 15.9)$ days using two relations: the $R - L$ relation⁶ and the $R_{\text{H}\beta} - (L, \mathcal{R}_{\text{Fe}})$ relation of $R_{\text{H}\beta} = 44.7 \ell_{44}^{0.45} 10^{-0.35 \mathcal{R}_{\text{Fe}}} \text{lt d}^7$, respectively. While the modest shortening factors ($10^{-0.35 \mathcal{R}_{\text{Fe}}} \lesssim 5$) could be explained by self-obscuration of the inner part of slim disks²⁸, this effect fails to account for large shortening factors. We note that the aliasing effects, which arise from seasonal gaps of long-term campaigns and observational errors, may randomly generate false-alarm LDRs. In § 5, we investigate the effects through Monte Carlo simulations. These simulations yield a false-alarm probability of $\lesssim 5 \times 10^{-5}$ listed in Tab. 2 and a corresponding significance level of $\gtrsim 4 \sigma$ if we set the lags of $\tau_{\text{H}\beta}^0 = 16.0 \text{lt d}$ from the $R_{\text{H}\beta} - (L, \mathcal{R}_{\text{Fe}})$ relation. Therefore, the LDR detections are robust in PHL 1092.

Fig. 3 shows the position of PHL 1092 in the $R_{\text{H}\beta} - (L, \mathcal{R}_{\text{Fe}})$ plane, revealing a complete deviation from the well-established BLR scaling relations. This points to a peculiar structure in this object different from the standard model of AGNs²⁹. Consequently, the conventional approach (Eq. 3 in § 1)^{5,29} for estimating SMBH masses becomes inapplicable to PHL 1092. Such an LDR phenomenon violates the causality of reverberations and has never been found in the past RM campaigns.

In order to explain the LDRs, we have to re-examine the validity of fundamental assumptions in reverberation physics. The most important one is that the ionizing source is treated as a point, namely, the point source approximation (PSA)², and the 5100 Å emission is conventionally used as a proxy for the ionizing emission. The PSA validity is examined in § 1 and § 6. The observed LDRs in PHL 1092 imply that the PSA is invalid, namely, the 5100 Å regions are extremely extensive, surpassing the BLR scale. This phenomenon triggers a series of significant challenges to the standard AGN model, as discussed in § 7. A fundamental issue is how to reconcile such extended structures with theoretical models of accretion disks³⁰. It is much beyond the scope of the present

paper to establish a definitive model for the case of PHL 1092, but we briefly discuss two possible mechanisms subsequently, which could jointly work for the LDRs.

First, we consider the extreme shortening of delays governed by accretion rates for the observed LDRs in PHL 1092. It is known that the 5100 Å radius scales with the accretion rate as $R_{5100} \propto (\dot{\mathcal{M}}/M_\bullet)^{1/3}$ in the regime of the Shakura-Sunyaev model (see Eq.23 in § 6). It increases until R_{5100} reaches the photon trapping radius, given by $R_{\text{trap}} \approx 10.4 \dot{\mathcal{M}}_3 M_8 \text{ lt}$ (see Eq. 22 in Ref.³¹), where $\dot{\mathcal{M}}_3 = \dot{\mathcal{M}}/10^3$ and $M_8 = M_\bullet/10^8 M_\odot$. In super-Eddington accretion disks, R_{5100} can be obtained by the effective temperature of $T_{\text{eff}} \approx T_c \tau_{\text{es}}^{-1/4}$ (rather than Eq. 22), where T_c denotes the temperature of the mid-plane and τ_{es} is the Thomson scattering depth³¹. Thus, we have the maximum R_{5100} radius of $R_{5100}^{\text{max}} = 15.8 M_8^{1/2} \text{ lt}$ that is independent of $\dot{\mathcal{M}}$ when the rates are extremely high as $\dot{\mathcal{M}}_3 \geq 0.95 M_8^{-1/2}$ (see Eq. 18-20 in Ref.³²). Conversely, for SEAMBHs, $R_{\text{H}\beta}$ decreases with $\dot{\mathcal{M}}$ (it correlates with \mathcal{R}_{Fe} as shown by Fig. 4 in Ref.²⁵). We expect a critical $\dot{\mathcal{M}}$ (or \mathcal{R}_{Fe}) at which $R_{5100}^{\text{max}} \approx R_{\text{H}\beta}$, namely, the observed delays of H β reverberations relative to 5100 Å continuum would vanish. For PHL 1092, this critical condition translates to $\mathcal{R}_{\text{Fe}} = 2.7 - 1.43 \log M_8$, where $\ell_{44} \approx 12.6$ (see Tab. 1). Taking $\tau_{\text{H}\beta}^0 = 15.9 \text{ days}$ from the $R_{\text{H}\beta} - (L, \mathcal{R}_{\text{Fe}})$ relation and $V_{\text{H}\beta} = 2270 \text{ km s}^{-1}$, we obtain $M_8 = 0.16$ from Eq. (3) (see Issue 1 in § 7, and § 8 about transfer functions for its order estimation). A lower limit of $\mathcal{R}_{\text{Fe}} \gtrsim 3.8$ is necessary for the case of $R_{\text{H}\beta} \sim R_{5100}$, which is much higher than the value 2.7 given in Tab. 1. Furthermore, such extreme Fe II emitters remain exceptionally rare in the SDSS database^{26,33}. Therefore, the extremely super-Eddington accretion scenario alone is insufficient to explain the LDRs.

Second, extra energy sources (EESs: Q_{extra}) heating the SMBH-disk are necessary to stretch the 5100 Å regions for the observed LDRs. Currently, continuum reverberations of accretion disks can be explained by reprocessing of X-rays as primary emissions in the lamp-post model^{34,35}. In the presence of EESs, Q_{extra} should be incorporated into the energy budget governing the effective

temperature of the SMBH-disk (T_{eff}) at a given radius $R^{9,10,36}$

$$\sigma_{\text{SB}} T_{\text{eff}}^4 = Q_{\text{vis}} + \frac{(1 - \mathcal{A})L_{\text{X}}}{4\pi R^2} \left(\frac{H}{R} \right) + Q_{\text{extra}}, \quad (1)$$

where σ_{SB} is the Stefan-Boltzmann constant, \mathcal{A} is the disk albedo, L_{X} is the X-ray luminosity from the hot corona (in the lamp-post model^{37,38}), Q_{vis} is the dissipation rates per area of gravitational energy of the SMBH-disk through viscosity in the standard model (see Eq. 21)³⁰, and H is the half-height of the disk. Here only the modified energy equation (Eq. 1) is listed for discussions, and a complete set of s@SMBH-disk equations is given by Ref.⁹. Q_{extra} alters the radial distribution of the effective temperature. Specifically, when Q_{extra} is sufficiently large relative to Q_{vis} , T_{eff} distribution becomes notably flatter than the well-known power law of $T_{\text{eff}} \propto R^{-3/4}$. Recent studies have shown that irradiated photons are efficiently thermalized locally within the disk^{39,40} and are re-radiated instantaneously at characteristic energies of their local environment. With Q_{extra} , both the ionizing photon field and the 5100 Å-emitting regions (R_{5100}^{\bullet}) are significantly extended, resulting in $R_{5100}^{\bullet} \gg R_{5100}$. In contrast, the broad-line region (BLR) is much less affected by Q_{extra} . This leads to a new structural configuration where $R_{5100}^{\bullet} > R_{\text{H}\beta}$ (with $R_{\text{H}\beta}$ being the BLR radius), corresponding to H β reverberating with a leading delay of $\tau_{\text{H}\beta}^{\ell} \approx (R_{\text{H}\beta} - R_{5100}^{\bullet}) \sin i / c < 0$, breaking down the PSA. Here i is inclinations of the SMBH-disk.

The Q_{extra} is suggested to originate from accreting sMBHs (previously denoted as accretion-modified stars as AMS⁴¹) embedded in the SMBH-disk (hereafter refer to s@SMBH-disk)^{8–10,41,42}. Fig. 4 illustrates the new scenario for the s@SMBH-disk and BLRs in PHL 1092. Actually, Q_{extra} depends on several factors⁹, including the total number of sMBHs, their spatial distribution across the disk, and their mass function. The total numbers may be inferred from BLR metallicity according to stellar evolution⁴³. Except for the alterations of T_{eff} , Q_{extra} also modifies the albedo of the disk surface – enhancing the reflection of X-rays from the corona. Both the reflected and reprocessed components in the SEDs are regulated by Q_{extra} . Consequently, the Q_{extra} -extended SMBH-disk is expected to be responsible for the observed LDRs in PHL 1092.

There is growing evidence supporting the existence of s@SMBH-disk, which is from optical variability in quasars^{44–46} and complemented by LIGO detections of gravitational waves (GWs) from events such as GW 190521^{44,47} and GW 231123⁴⁸. These two GW events imply that their progenitors required a dense environment—specifically, AGN accretion disks—for formation. This is because such events cannot be explained by normal stellar evolution⁴³; instead, they likely form via either rapid growth through accretion^{44,49} or hierarchical mergers^{50–52}. Recent discoveries further reinforce this picture: the detection of millihertz (mHz) quasi-periodic oscillations (QPOs) in the actively accreting SMBH of 1ES 1927+654 supports the presence of satellite black holes orbiting the central SMBH⁵³, as do newly identified quasi-periodic eruptions (QPEs)^{54–58} associated with tidal disruption events⁵⁹. This body of evidence is consistent with our detection of leading delays of $H\beta$ reverberations in PHL 1092. Other potential models for explaining LDRs are briefly discussed in § 9, including 3D winds acting as the broad-line region (BLR), anisotropic radiation from the accretion disk, extended winds from super-Eddington accretion, and even complex turbulence differing from the standard Shakura-Sunyaev model. None of these models can fully explain the observed LDRs, and those that come close require highly specific configurations or conditions. We therefore favor AMS-driven heating as a nascent and parsimonious mechanism for generating LDRs – one that is supported by observational hints^{44,45,47,48}.

Our monitoring campaign of PHL 1092 reports the first detection of leading delays in the reverberations of the broad $H\beta$ line relative to the 5100 Å continuum. This finding indicates that the optical continuum-emitting regions extend beyond the BLRs. This structural configuration deviates from the standard AGN model and fundamentally undermines the conventional BLR-based methodology for estimating SMBH masses. Furthermore, there are a small number of PHL 1092 analogs from our SEAMBH campaign, though these objects exhibit slightly more complex behaviors (see Issue 3 in § 7). This suggests that such systems are neither common nor rare. The LDRs suggesting EESs powered by accretion of the sMBHs widely distributed over the SMBH-disk, provide compelling observational evidence for the existence of s@SMBH-disk. If such accretion

disks are ubiquitous in AGNs but vary in the number of embedded sMBHs, the shortening of $\tau_{H\beta}$ should extend continuously to the regime of leading delays. We thus expect the analogs to fill the gap between PHL 1092 and the $R_{H\beta} - (L, \mathcal{R}_{Fe})$ relation in Fig. 3. Additionally, advancements in optical and near-infrared interferometry, such as the future Kilometers Baseline Interferometers⁶⁰, are anticipated to directly image s@SMBH-disk systems. Issue 6 in § 7 briefly discusses the evolution of sMBHs inside the SMBH-disk for observational diverse properties in light of variations of broad emission lines and continuum. Complementary to this, GW detections from nearby AGNs via missions such as LISA¹¹/Tianqin¹², the Einstein Telescope (ET)¹³, or space-based detection networks⁶¹ could further confirm the presence of these systems.

Correspondence Correspondence and requests for materials should be addressed to Jian-Min Wang (email: wangjm@ihep.ac.cn).

Acknowledgements The authors are grateful to three referees for their helpful reports clarifying ambiguous points and motivating us to think about the potential explanations of the LDRs. This research is supported by grants NSFC-12333003, -92476203, -12521005, -12573016, the National Key R&D Program of China (2021YFA1600404, 2023YFA1607903, and 2023YFA1607904), the National Science and Technology Major Project (2024ZD0300303), the China Manned Space Project (CMS-CSST-2025-A07), and the Strategic Priority Research Program of the Chinese Academy of Sciences (XDB1160202).

Author Contributions JMW is the Principle Investigator of the SEAMBH project. He discovered the LDRs, made the theoretical model of the LDRs and wrote the manuscript. CH, YJC, YYSS, YLW, HZ, WJG, SY, ZHY and JA made observations, and CH and YJC reduced data. YJC, YRL and JMW made all LC fittings through MICA. YYSS and JMW made Monte Carlo simulations on inhomogeneity of ionizing variations of extended sources, and found the non-concordant reverberations. PD and JMW estimated Fe II contamination to $H\beta$ line. All the authors discussed the contents of the paper.

Competing Interests The authors declare that they have no competing financial interests.

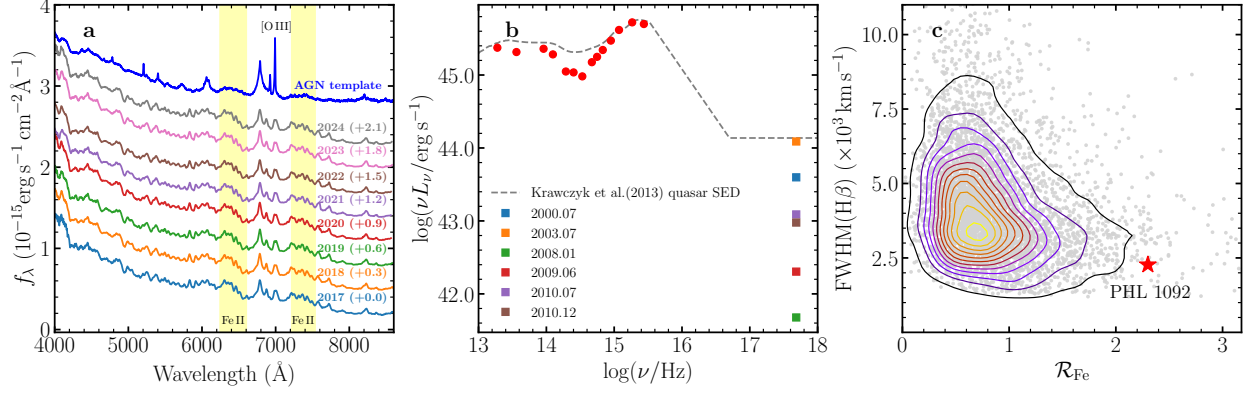


Figure 1: Panel **a**: Annual mean spectra of PHL 1092 (in the observer’s frame). Spectral fluxes have been vertically offset for clarity. Compared with the Sloan Digital Sky Survey (SDSS) quasar template (blue line)⁶², PHL 1092 exhibits prominent Fe II features and weak [O III] λ 5007 Å line emission—characteristics that distinguish it from normal quasars. The yellow shaded regions highlight the optical Fe II lines. Panel **b**: SED of PHL 1092 (solid line) compared with the mean spectral energy distribution (SED) of luminous quasars (dotted line)⁶³. Its SED is significantly bluer (i.e., has a steeper continuum) than the quasar mean SED. Its X-ray flux varies by more than two orders of magnitude²². SED data sources: ultraviolet (UV) from GALEX, optical from SDSS, near-infrared (NIR) from 2MASS, and mid-infrared (MIR) from WISE. Panel **c**: Position of PHL 1092 in the \mathcal{R}_{Fe} -FWHM($\text{H}\beta$) diagram of the SDSS data²⁶, exhibiting PHL 1092 as an extreme quasar.

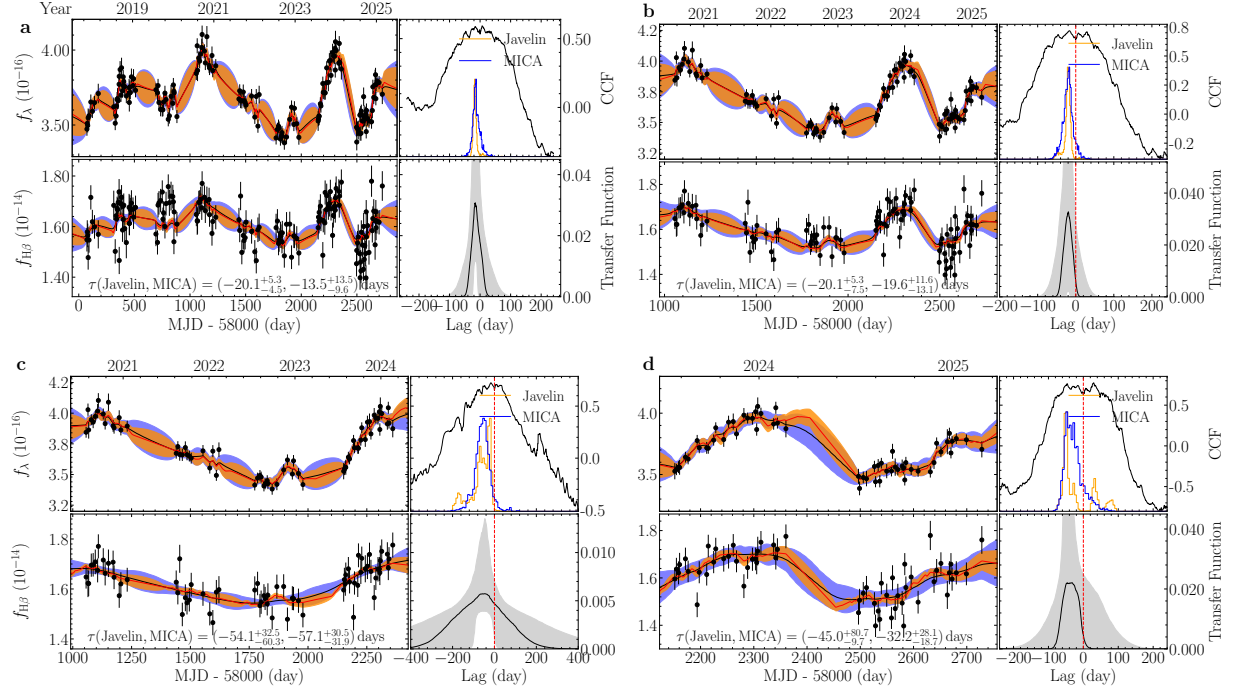


Figure 2: Panels **a–d** display the LCs of the 5100 Å continuum and H β line across different observational periods. The cross-correlation function (CCF) reveals a strong correlation between the 5100 Å continuum and H β line variations. Given the presence of multiple peaks in the CCF results, we used two independent methods —JAVELIN and MICA—to determine the reverberation delays. The delay results derived from JAVELIN (yellow) and MICA (blue) are in good agreement with each other. The red dotted lines mark $\tau_{H\beta} = 0$ (i.e., zero delay between H β and the 5100 Å continuum). The detected LDRs are consistent across all observational periods.

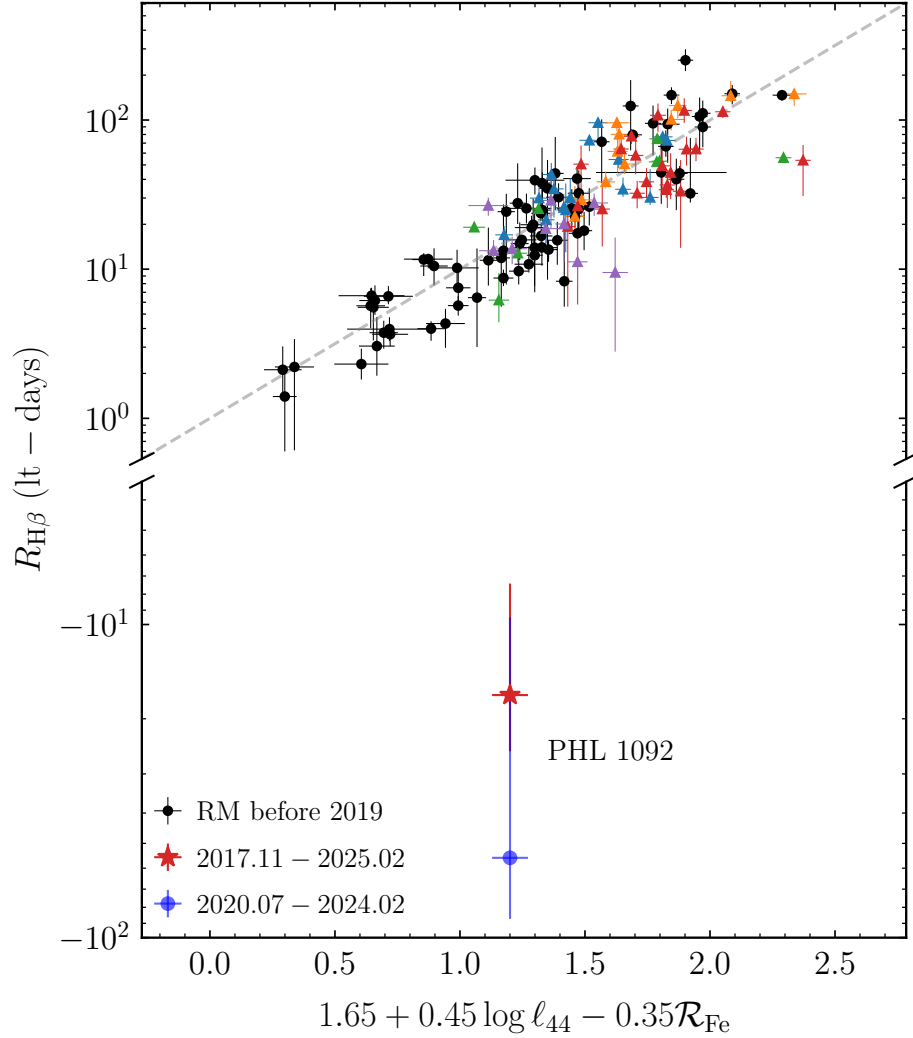


Figure 3: The position of PHL 1092 in the $R_{H\beta} - (L, \mathcal{R}_{Fe})$ plane demonstrates that this object completely deviates from the known structures of AGNs. Such a violation of reverberation causality requires additional energy sources (EESs) to extend the SMBH-disk. RM data prior to 2019 (black points) are summarized in Ref.⁷, which includes measurements from^{4,6,19,64} and other relevant literature (see the complete reference list in Ref.⁷). Post-2019 RM points (color triangles) are from projects of LAMP⁶⁵ (in purple), SEAMBH^{66,67} (in blue and orange), SAMP⁶⁸ (in red), and MAHA (in green)⁶⁹ with available \mathcal{R}_{Fe} measurements. The dashed lines are adopted from Ref.⁷.

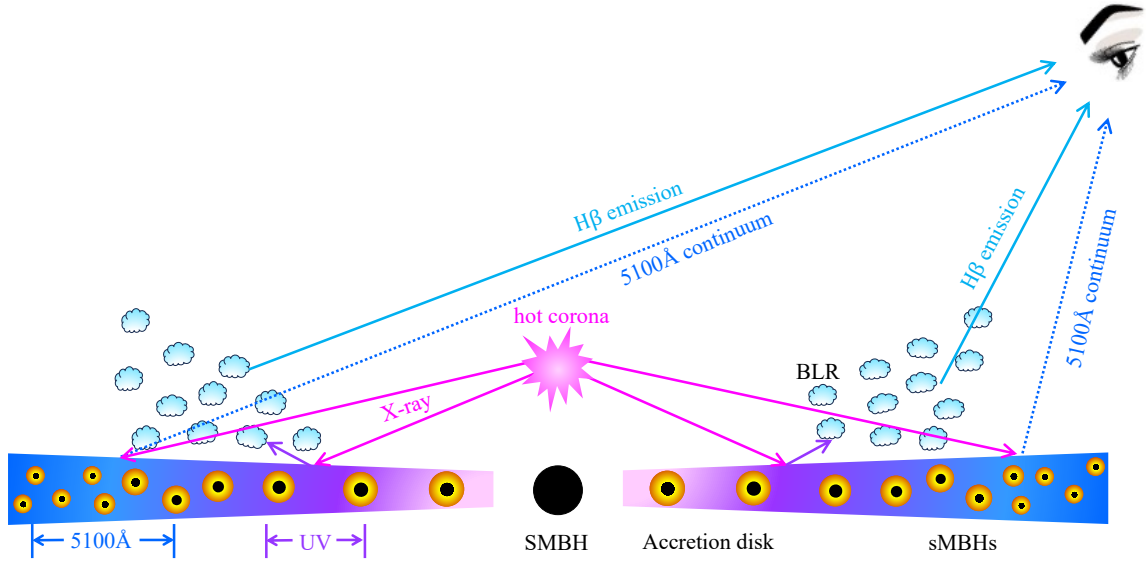


Figure 4: This diagram illustrates the SMBH-disk with embedded stellar-mass black holes (sMBHs) — a system denoted as s@SMBH-disk—proposed to explain the observed phenomena in PHL 1092. The sMBHs are represented as black dots surrounded by gradient yellow cocoons. The total energy budget of the SMBH-disk must include energy contributions from the sMBH accretion altering the radial distribution of the disk’s effective temperature (T_{eff}). This gives rise to a large extension of the 5100 Å regions so that the BLR clouds (in shallow blue) are located within the former, appearing the observed leading delays of broad $H\beta$ line reverberations. The sMBHs are growing with inward migration but their number density decreases because of hierarchical mergers.

Table 1: Information of PHL 1092 and observations

α_{2000}	δ_{2000}	redshift	M_r	L_{5100}	\mathcal{R}_{Fe}	FWHM	N_{sp}	Comparison stars	
				(erg s ⁻¹)		(km s ⁻¹)		R_*	P.A.
01 39 55.76	+06 19 22.55	0.396	16.8	1.26×10^{45}	2.7	2270	157	129''.9	200.6°

M_r is the r -band magnitude.

N_{sp} is the numbers of spectroscopic observing epochs.

R_* is the angular distance to the targets and P.A. is the position angle.

 Table 2: H β reverberation results of 8-year campaign of PHL 1092

Duration	Variability amplitudes*		Time lags ($\tau_{\text{H}\beta}^{\ell}$)				
	$F_{\text{var}}(5100 \text{ \AA})$	$F_{\text{var}}(\text{H}\beta)$	JAVELIN	MICA	Mean	p	Significance
	(%)	(%)	(day)	(day)	(day)		(σ)
2017.11–2025.02	4.36 ± 1.00	4.19 ± 0.58	$-20.1^{+5.3}_{-7.5}$	$-13.5^{+13.5}_{-9.6}$	$-16.8^{+9.4}_{-8.6}$	5×10^{-5}	4.1
2020.07–2024.02	5.35 ± 1.77	3.59 ± 0.8	$-54.1^{+32.5}_{-60.3}$	$-57.1^{+30.5}_{-31.9}$	$-55.6^{+31.5}_{-46.1}$	2×10^{-4}	3.7
2020.07–2025.02	5.13 ± 1.42	4.58 ± 0.74	$-20.1^{+5.3}_{-7.5}$	$-19.6^{+11.6}_{-13.1}$	$-19.9^{+8.5}_{-10.3}$	2×10^{-4}	3.7
2023.07–2025.02	4.82 ± 1.70	6.03 ± 0.94	$-45.0^{+80.7}_{-9.7}$	$-32.2^{+28.1}_{-18.7}$	$-38.6^{+54.4}_{-14.2}$	4×10^{-4}	3.4

F_{var} : is calculated using Eq. (5) and uncertainties according to Ref.⁷⁰.

Mean: is the arithmetic mean values of JAVELIN and MICA measurements.

p : is the LDR probability due to aliasing effects and the according significance. We generated 2×10^4 pairs of LCs for 2017.11–2025.02, 5000 pairs for other periods.

Methods

1 Overview of RM AGNs and conventional RM physics

1.1 Campaigns AGNs are prominently characterized by broad emission lines⁶² (see extensive review in the textbook²⁹) as well as in high- z quasars^{71,72}. BLRs, which are photoionized by radiation from the SMBH-disk, are filling with numerous discrete clouds that emit emission lines. The lines are broaden by orbiting motion around the central SMBH, but they are spatially unresolved so far except for a few AGNs observed by GRAVITY/VLTI along with spectroastronomy (note GRAVITY results are not spatially resolved images of BLRs)⁷³. Fortunately, the BLR clouds reverberate in response to continuum variability of the SMBH-disk. The resulting echoes of broad emission lines convey invaluable information about the spatial distributions and kinematics of the BLRs¹⁻³ enabling the measurement of SMBH masses through RM campaigns⁵. Since the 1980s, astronomers have initiated RM campaigns to probe the kinematics and structure of BLRs (see a classical review on the RM technique³). To date, approximately ~ 300 AGNs have been studied, which are contributed from several major programs. According to methods of spectral calibrations, we list them:

- RM campaigns with calibrations through comparison stars
 - Steward PG program at Arizona (only 17 objects)⁴ with the Bok 2.3 m telescope,
 - Super-Eddington Accreting Massive Black Holes (SEAMBHs) at Yunnan Observatory and Centro Astronómico Hispano-Alemán (CAHA) Observatory (SEAMBHs: ~ 60)^{7,32,66,67,74,75} with the Lijiang 2.4 m and the CAHA 2.2 m telescopes,
- RM campaigns with calibrations through [O III] λ 5007Å
 - AGN Watch (10 objects)*, Ohio State Project (~ 25)⁷⁶⁻⁷⁹ with several 1.5 m and 2 m

*<https://www.asc.ohio-state.edu/astronomy/agnwatch/>

telescopes,

- Lick AGN Monitoring Project (LAMP: ~ 60)^{65,80,81} with the Shane 3.0 m telescope,
- Monitoring AGNs with H β Asymmetry (MAHA) projects at Wyoming Infrared Observatory (~ 35)^{64,69,82} with the WIRO 2.3 m telescope,
- the Seoul National University AGN Monitoring Project (~ 30)⁶⁸ with the Shane 3.0 m telescope
- and multiple fiber-fed spectrograph campaigns: Oz-DES Project (~ 8)⁸³ and SDSS-RM Project (~ 80)⁸⁴ with 4 m and 2.5 m telescopes, respectively.

In Fig. 3, only objects with subtraction of host contamination are plotted. These RM campaigns have greatly advanced the understanding of BLRs.

SEAMBH campaigns, focusing on AGNs with high Eddington ratios, have been conducted using the CAHA 2.2 m and Lijiang 2.4 m telescopes. Target AGNs are selected primarily based on two key features: high values of \mathcal{R}_{Fe} and high accretion rates \mathcal{M} (see Eq. 4). For discussions of PHL 1092 analogs, refer to Issue 3 in § 7. Phenomena of leading delays in H β reverberations in AGNs are neither common nor extremely rare. Despite of these objects we are not able to make a significant statistics of the phenomenon from this heterogeneous sample.

To date, over one million quasars have been identified⁸⁵. Although most of them have been photometrically monitored by ZTF⁸⁶, however, only about a few 10^{-4} of quasars have been mapped by campaigns, moreover no more than 20 AGNs and quasars have been spectroscopically monitored continually with high cadences longer than 7-8 years (except for NGC 5548⁸⁷). Ref.⁴ performed the 7 year campaigns of 17 PG quasars, but cadences of most targets are quite poor. As a result, the understanding of the inner structures of AGNs is extremely limited. Long term campaigns of RM with high cadence through 2 m telescopes are necessary to reveal anomalous reverberations of H β line as we briefly discuss PHL 1092 analogs in § 7. So far, the SEAMBH cam-

paings are the longest RM campaigns (some of them are 8-9 years) with high and homogeneous cadence then. In the meanwhile, large telescopes are also necessary to explore details of spatially inhomogeneous variations of ionizing sources in these analogs. Although the campaigns are very costly in terms of observation time and human resources, it provides significant scientific returns for us revealing not only various versions of inner structures of AGNs beyond their standard model but also gravitational waves as fundamental physics. It is just for 2 m telescopes, we would like to emphasize here, that the significant goals can be achieved by discovering diverse behaviors of $H\beta$ line reverberations in AGNs.

The validation of significant reverberations typically relies on the maximum cross-correlation function (CCF) coefficient, denoted as r_{\max} . In practice, r_{\max} is a complex function influenced by multiple factors: the transfer function of the system, the observational cadence and its uniformity, seasonal gaps in data, and the total number of observational points. While no strict universal criterion exists for validating reverberations, a common threshold adopted in the literature is $r_{\max} \gtrsim 0.5$ ⁸⁰. To contextualize this threshold, we checked r_{\max} values in several popular studies^{4,65,76,80}. Notably, even datasets with suboptimal cadence have been shown to yield $r_{\max} \sim 0.8 - 0.9$ provided the total number of data points is not many. For the present work, the measured $r_{\max} \sim 0.7$ is well above the typical acceptance threshold. This value supports a robust detection of reverberations, consistent with the standards established in the aforementioned references.

1.2 Standard physics of reverberations The standard AGN model consists of three key components: the accretion disk, the BLR, and the dusty torus²⁹. In general, the radiation-dominated region of the accretion disk is significantly smaller than the BLR. Additionally, results from infrared RM campaigns indicate $R_{H\beta} \approx (0.1 \sim 0.2) R_{\text{torus}}$, where R_{torus} denotes the inner radius of the dusty torus⁸⁸. These three components may represent distinct regions (each governed by unique physical processes) of a continuous gaseous disk – permeated with clumps – that extends from the inner to outer scales of the AGNs⁸⁹. Alternatively, they could be physically linked through the tidal capture of clumps^{90,91}.

A robust relation between the BLR size and optical luminosity has been established for sub-Eddington accreting AGNs^{4,6,65,68}, but super-Eddington AGNs have shortened H β lags depending on accretion rates compared with the same luminosity AGNs^{7,19,64,74}. We define the dimensionless accretion rate as $\dot{\mathcal{M}} = \dot{M}_\bullet / \dot{M}_{\text{Edd}}$, where \dot{M}_\bullet is mass accretion rates of the central SMBH, $\dot{M}_{\text{Edd}} = L_{\text{Edd}}/c^2$ is the critical rates corresponding to the Eddington luminosity of $L_{\text{Edd}} = 4\pi G M_\bullet c / \kappa_{\text{es}}$, and κ_{es} is the opacity of electron scatterings. SEAMBHs are defined as $\dot{\mathcal{M}} \gtrsim 3$ above which the inner structure of accretion disks can no longer be adequately described by the Shakura-Sunyaev model⁹². It is well understood that \mathcal{R}_{Fe} is a good proxy of accretion rates⁹³ (see also Fig. 4 in Ref.²⁵). Super-Eddington AGNs occupy about 1/3 of PG quasars known as narrow line Seyfert 1 galaxies, and similar fractions of SEAMBHs in SDSS quasars was found in light of \mathcal{R}_{Fe} ³³. The BLR scaling relation is expressed as

$$\frac{R_{\text{H}\beta}}{R_g} = \begin{cases} 5.8 \times 10^4 \ell_{44}^{0.53} M_7^{-1} & (\text{for } \dot{\mathcal{M}} \leq \dot{\mathcal{M}}_C), \\ 7.7 \times 10^4 \ell_{44}^{0.45} M_7^{-1} 10^{-0.35 \mathcal{R}_{\text{Fe}}} & (\text{for } \dot{\mathcal{M}} > \dot{\mathcal{M}}_C), \end{cases} \quad (2a)$$

where $\dot{\mathcal{M}}_C \approx 11$ is the critical rates, $R_g = GM_\bullet/c^2 = 1.5 \times 10^{12} M_7 \text{ cm}$ is the gravitational radius, G is the gravitational constant and $M_7 = M_\bullet / 10^7 M_\odot$ is the SMBH mass. This indicates that the BLR shrinks with increases of $\dot{\mathcal{M}}$, and sometimes shortened by factors up to ~ 8 (and $\dot{\mathcal{M}} \sim 900$) so far⁶⁴ from the SEAMBH campaigns.

Comparing with the disk radius (Eq. 23), we find that $R_{5100} \ll R_{\text{H}\beta}$, namely, the PSA is valid in sub-Eddington AGNs, underpinning the widely used methodology for estimating SMBH masses

$$M_\bullet = f_{\text{BLR}} \frac{R_{\text{H}\beta} V_{\text{H}\beta}^2}{G} \approx 2.0 \times 10^6 \tau_{10} V_3^2 M_\odot, \quad (3)$$

where f_{BLR} is the virial factor ($f_{\text{BLR}} = 1$ is taken for SEAMBHs^{19,94}), $V_{\text{H}\beta}$ is the full-width-half-maximum (FWHM) of H β profiles, $\tau_{10} = \tau_{\text{H}\beta} / 10 \text{ days}$ and $V_3 = V_{\text{H}\beta} / 10^3 \text{ km s}^{-1}$. The dimensionless accretion rates can be expressed by

$$\dot{\mathcal{M}} \approx 20.1 \left(\frac{\ell_{44}}{\cos i} \right)^{3/2} M_7^{-2}, \quad (4)$$

in light of the Shakura-Sunyaev model^{30,74}. In addition to the assumption that motion of clouds is virialized, Eq. (3) also strongly depends on the PSA, specifically, the condition $R_{5100} \ll R_{H\beta}$. However, this approximation is not universally valid, in particular, for extreme super-Eddington accreting massive black holes (SEAMBHs), R_{5100} can become comparable to the size of the BLR, violating the PSA. This caveat should be borne in mind.

1.3 Non-point source effects When the PSA breaks down, what reverberation behaviors emerge? This question is addressed using toy models of extended ionizing sources in § 4. In this model, the 5100 Å/ionizing sources regions are so extensive that the reverberations of broad H β line emissions arise from twice convolutions of independent transfer functions of the BLR and continuum regions [denoted by $\Psi_{H\beta}$ and Ψ_{ion} in Eq. (27), respectively].

This double convolution causes the H β line LC to exhibit non-concordant behaviors, reflecting composite responses from different regions of the BLR. In other words, the H β line does not reverberate straightforwardly with respect to the continuum. Notably, spatial inhomogeneities of the ionizing source components further complicate these behaviors. These processes not only cover the smooth effects of BLR geometries but also the effects of continuum geometry and spatial distributions. For more realistic models, reverberation behaviors are expected to be even more complex. This phenomena of non-concordant behaviors resulting from ionizing photon propagation of non-point source (NPS) to the extensive BLR regions are referred as the NPS effect in this paper. Details are provided in § 4.

1.4 Anomalous behaviors of reverberations While most AGNs studied via RM exhibit regular reverberation behavior, anomalous reverberations have been detected in a small number of objects. For instance, the AGN STORM campaign of NGC 5548 revealed that the broad H β line failed to reverberate in response to 5100 Å continuum variations over a ~ 50 day period⁹⁵. A similar phenomenon was observed in PG 1613+658 during the time interval JD 2457000 + (1750–2000) as part of the MAHA campaign⁶⁹. Such anomalous reverberations may arise from inhomogeneities

in either the broad-line region (BLR) or the ionizing source. Furthermore, NGC 5548 follows a scaling relation of $R_{\text{H}\beta} \propto L_{5100}^{0.8-0.9}$ —with substantially larger scatter and a significantly steeper slope compared to the canonical $R_{\text{H}\beta} \propto L_{5100}^{0.5}$ relation established over the past three decades of RM campaigns⁸⁷. Mrk 817⁹⁶ and NGC 7469⁹⁷ have also displayed anomalous reverberation behaviors (potentially attributable to the NPS effects discussed in § 4). However, the conventional BLR-based method for SMBH mass estimation still yields valid results for these objects. The reverberation behavior of PHL 1092 differs fundamentally from all the aforementioned cases.

2 Observations and data reduction

2.1 Observations The 2.2 m telescope at the CAHA Observatory was used for the monitoring campaigns. Detailed procedures are provided in Ref.^{66,67}, however, a brief overview is presented here for the reader’s convenience. Each night, broadband images of the target (PHL 1092) were first acquired. A long slit—with a projected width of 3.''0 — was then carefully aligned, and spectra of both the target and a nearby non-variable comparison star were obtained simultaneously. To minimize slit-induced light loss (critical for high-precision flux calibration), the target and the comparison star were centered in the slit with typical positional accuracy: the offset from the slit center along the width direction was less than 0.5 pixels (corresponding to a projected offset of 0.''265). Observational details for the target and the comparison star are given in Tab. 1.

Three 120-second exposures of Johnson *V*-band images were typically acquired per night. Image reduction followed standard IRAF procedures. Fluxes of the target and the comparison star were measured via a circular aperture (2.''65), with differential magnitudes calculated relative to 7 other stars in the 9.''7 × 9.''7 field.

PHL 1092 spectra were taken with the Calar Alto Faint Object Spectrograph (CAFOS) using Grism G-200 for its relatively high efficiency. The resulting spectrum covers 4000 – 8500 Å, with a dispersion of 4.47 Å pixel^{−1}. Two 1800-second exposures were taken per night, and the typical

signal-to-noise ratio (S/N) per pixel for a single exposure is ~ 40 at rest-frame 5100 \AA . One or two spectrophotometric standards were observed each night during dusk and/or dawn, weather and time permitting.

2.2 Data reduction Spectra were reduced in IRAF via standard procedures: bias removal, flat-fielding, wavelength calibration, and 1D extraction. Extraction apertures were uniformly large ($10.''6$) to minimize light loss, particularly on nights with poor seeing. The target’s flux calibration used a sensitivity function derived from the comparison star, as detailed below.

First, on several clear nights, the comparison star was flux-calibrated via standard IRAF procedures using the night’s spectrophotometric standards. Second, these calibrated spectra were combined to produce a fiducial comparison star spectrum. Third, for each exposure, a Legendre polynomial was fitted by comparing the comparison star’s extracted count spectrum to the fiducial spectrum. This polynomial acts as the sensitivity function, accounting for atmospheric effects, slit loss, and instrument response. Telluric absorption was corrected using the comparison star as a telluric standard^{4,98}. Finally, each spectrum of the target was flux-calibrated with the corresponding sensitivity function; the two nightly calibrated spectra were combined to form a single-night spectrum for subsequent measurements and analysis.

Flux calibration accuracy is better than 3% in Ref.⁶⁶. The comparison star’s V -band LC is shown in Fig. 5a. Its differential magnitude scatter is only 0.013 mag, far smaller than the target’s variations which ensures spectroscopic flux calibration accuracy.

2.3 Seeing influence From V -band images, we derived FWHMs of surface brightness distributions for the target and the comparison star (Fig. 5b and 5c). Comparison star FWHMs serve as seeing measurements. Target FWHMs are nearly identical to that of the comparison star, indicating negligible host starlight contribution. Notably, continuum and $H\beta$ LC deviations from DRW fits (Fig. 6) show no correlation with seeing—confirming spectroscopic flux calibration is unaffected by seeing variations (due to our broad slit width and minimal host contribution). Deviations are

driven by calibration accuracy.

2.4 Light curve measurements Following the traditional method^{4,99}, we obtain the broad H β line and continuum LCs through integrating over a range of relevant wavelengths. The window of 4810–4900 Å (in the rest frame) was set for the H β line. A straight line was defined by the two continuum windows located on both sides of the H β (4680–4710 Å and 5070–5100 Å, chosen to have minimum contribution of the Fe II line emissions), and then the flux above this straight line was integrated in the emission-line window. The average flux in the redward continuum window was calculated as the integrated 5100 Å flux (F_{5100}). Fig. 2 shows the LCs of different periods.

The Fe II LC, shown in Fig. 7, is also measured by the integration method similar to Ref.⁸¹, as done for the H β line. The windows of 3795–3810 Å and 4690–4705 Å are used for defining the continuum, and the window of 4434–4584 Å is set for integrating the Fe II flux (all three windows are in the rest frame). Note that this integration window of Fe II is narrower than the window of 4434–4684 Å used for defining the Fe II flux for calculating the \mathcal{R}_{Fe} , where the 4584–4684 Å window is masked here avoiding the possible influence of He II emission line.

Spectral fitting method is employed to obtain LCs for campaigns with high spectral resolution spectrographs. It is necessary for the lines which blended with others (such as He II), or in the cases that the host starlight is strong to contaminate the AGN continuum (the host is weak in PHL 1092). However, it will introduce extra uncertainties by the imperfect modeling⁶⁶. We did this excise though the CAFOS resolution is only $\lambda/\Delta\lambda \sim 300$ since we took the slit width of 3'' (see § 2.1). The results yielded by the spectral fitting is consistent with that of the integrations but with larger uncertainties in some degrees.

2.5 Error bars Observed error bars consist of two parts $\delta_{\text{obs}} = \sqrt{\delta_{\text{sys}}^2 + \delta_{\text{meas}}^2}$, where δ_{sys} and δ_{meas} are the systematic and measured error bars, respectively. Here we adopt two methods to estimate the systematic uncertainties, namely, the median filter and MICA fit. Following the median-filter approach^{76,80}, we smooth each LC with a five-point sliding median to capture the long-term trend.

Subtracting this median-smoothed curve from the original, we compute the standard deviation of the residuals σ_{Med} . The smoothed curve and residuals are shown in Fig. 6. We adopt $\sigma_{\text{Med}} = \delta_{\text{sys}}$ as an epoch-independent systematic uncertainty. Across our eight-year data set, the resulting systematic uncertainties for the continuum and H β line are approximately 1.2% and 2.7% of the respective fluxes, consistent with the calibration accuracy being better than 3%.

For the MICA fitting, δ_{sys} is treated as a free parameter during the LC modeling[†]. Applying to our data, we obtain the systematic uncertainties of about 1.3% and 3.8% for the continuum and H β , respectively. The MICA-derived δ_{sys} is slightly larger than the median-filter estimate because the long-term variability patterns of the continuum and H β are not perfectly matched (eg, MJD 2250 in panel **a** of Fig. 2, which are caused by non-concordant reverberations of spatially inhomogeneous variations of extended ionizing sources). To achieve a statistically consistent fit (reduced $\chi^2 \approx 1$), MICA necessarily inflates the systematic term. Considering these limitations, we adopt the median-filter estimate as our fiducial δ_{sys} for LCs.

2.6 Variations We use the popular methods¹⁰⁰ to calculate LC characteristics of the continuum and the H β emission line. They are

$$F_{\text{var}} = \frac{(\sigma^2 - \Delta^2)^{1/2}}{\langle F \rangle}, \quad (5)$$

where

$$\sigma^2 = \sum_{i=1}^N \frac{(F_i - \langle F \rangle)^2}{(N-1)}, \quad \Delta^2 = \sum_{i=1}^N \frac{\Delta_i^2}{N}, \quad \langle F \rangle = \sum_{i=1}^N \frac{F_i}{N}, \quad (6)$$

and the error bar of F_{var} is given by⁷⁰

$$\sigma_{\text{var}} = \frac{1}{F_{\text{var}}} \left(\frac{1}{2 \times N} \right)^{1/2} \frac{\sigma^2}{\langle F \rangle^2}, \quad (7)$$

where N is the total number of data, F_i is the flux of the i -th observation, and Δ_i is the uncertainty of F_i . We denoted F_{var}^{5100} , $F_{\text{var}}^{\text{combine}}$ and $F_{\text{var}}^{\text{H}\beta}$ as variation amplitudes of the LCs for the 5100 Å continuum, the combined continuum and broad H β line.

[†]More details of MICA can be found in this URL: <https://mica2.readthedocs.io/en/latest/>.

2.7 Amplitudes of Fe II variations Considering difficulties that Fe II variations are too small to measure, we estimate an intrinsic relation of Fe II from H β variations as followings. If the BLRs are virialized in the central SMBH potential, the Fe II regions are $R_{\text{Fe}} \approx (V_{\text{H}\beta}/V_{\text{Fe}})^2 R_{\text{H}\beta}$, where $V_{\text{H}\beta}$ and V_{Fe} are the FWHMs of H β and Fe II lines. The relative variations of H β line are given by $\delta F_{\text{H}\beta} = \Delta F_{\text{H}\beta}/\langle F_{\text{H}\beta} \rangle$, where $F_{\text{H}\beta}$ and $\Delta F_{\text{H}\beta}$ are the steady/mean fluxes of the line and its variations, respectively. Observationally, we take $\delta F_{\text{H}\beta} = (F_{\text{max}} - F_{\text{min}})/\langle F_{\text{H}\beta} \rangle \approx 3\sigma$, F_{max} and F_{min} are the maximum and minimum of H β line variations (corresponding to 1.5σ deviations from the mean values of fluxes), respectively.

According to photoionization of the BLR, we have $\Delta F_{\text{H}\beta} = \Delta F_{\text{ion,H}\beta} (\Delta t_{\text{ion}}/\Delta t_{\text{H}\beta})$, where $\Delta F_{\text{ion,H}\beta}$ is the variations of the H β ionizing fluxes, and $(\Delta t_{\text{ion}}, \Delta t_{\text{H}\beta})$ are the variation timescales of the ionizing sources and H β line, respectively. We have

$$\delta F_{\text{H}\beta} = \left(\frac{\Delta F_{\text{ion,H}\beta}}{F_{\text{H}\beta}} \right) \left(\frac{\Delta t_{\text{ion}}}{\Delta t_{\text{H}\beta}} \right). \quad (8)$$

In light of the lamp-post model, the ionizing photons are the reprocessed emissions of X-ray photons by the disk surface. Given ξ_X is the reprocessing coefficient, we have $F_{\text{H}\beta} = \xi_X L_X / 4\pi R_{\text{H}\beta}^2 c$ and $\Delta F_{\text{ion,H}\beta} = \xi_X \Delta L_X / 4\pi R_{\text{H}\beta}^2 c$, yielding $\Delta F_{\text{ion,H}\beta} / F_{\text{H}\beta} = \Delta L_X / L_X$, where L_X and ΔL_X are X-ray luminosity and its variations, respectively. Similarly, we have the relative variations of the Fe II,

$$\delta F_{\text{Fe}} = \left(\frac{\Delta F_{\text{ion,Fe}}}{F_{\text{Fe}}} \right) \left(\frac{\Delta t_{\text{ion}}}{\Delta t_{\text{Fe}}} \right) = \left(\frac{\Delta t_{\text{H}\beta}}{\Delta t_{\text{Fe}}} \right) \delta F_{\text{H}\beta}, \quad (9)$$

where we use a similar relation of $\Delta F_{\text{ion,Fe}} / F_{\text{Fe}} = \Delta L_X / L_X$. This shows the relations between H β and Fe II variations in the framework of the lamp-post model. Considering that the $(\Delta t_{\text{H}\beta}, \Delta t_{\text{Fe}}) \approx (R_{\text{H}\beta}, R_{\text{Fe}})/c$ and the virialization relations, we have

$$\delta F_{\text{Fe}} = \left(\frac{V_{\text{Fe}}}{V_{\text{H}\beta}} \right)^2 \delta F_{\text{H}\beta} \approx 0.2 \delta F_{\text{H}\beta}, \quad (10)$$

for PHL 1092, where $(V_{\text{H}\beta}, V_{\text{Fe}}) \approx (2270, 1054) \text{ km s}^{-1}$ are from Fig. 8. We thus expect the Fe II's intrinsic variations of $\delta F_{\text{Fe}} \approx 3\%$ only from the observed $\delta F_{\text{H}\beta} \approx 15\%$. Fig. 7 shows that the scatters of Fe II variations are dominated by the system errors, which are consistent with the rough

assessments of the Fe II variations by Eq. (10). Actually, the H β LCs could be contaminated by the Fe II line as the systematic errors, however, its contamination to H β variations is small enough shown by Eq. (10) in PHL 1092.

It is worth of noting that our SEAMBH campaigns¹⁰¹ successfully measured Fe II reverberations in 9 narrow-line Seyfert 1 galaxies (NLS1s). We find that these objects have $\delta F_{\text{Fe}} \sim \delta F_{\text{H}\beta}$ from Eq. (10) in light of $V_{\text{H}\beta} \sim V_{\text{Fe}}$ listed in Tab. 2 of Ref.¹⁰¹. Independently, $\delta F_{\text{Fe}} \sim \delta F_{\text{H}\beta}$ indeed holds from the LCs in the nine NLS1s¹⁰¹. It is clear from $V_{\text{Fe}}/V_{\text{H}\beta}$ that PHL 1092 has much larger structures of Fe II line regions compared with other NLS1s. Other two successful measurements of Fe II reverberations¹⁰² have been done for NGC 4593 and Mrk 1511, in which $\delta F_{\text{H}\beta} \sim (60\%, 30\%)$, and $\delta F_{\text{Fe}} \sim (40\%, 25\%)$ from their LCs, respectively. The FWHMs of NGC 4593 and Mrk 1511 were found that $V_{\text{H}\beta} = (4395 \pm 362, 4171 \pm 137) \text{ km s}^{-1}$ and $V_{\text{Fe}} = (3330 \pm 153, 3128 \pm 143) \text{ km s}^{-1}$ from the Boroson & Green template of Fe II lines, or $V_{\text{Fe}} = (5044 \pm 176, 4459 \pm 116) \text{ km s}^{-1}$ from the Véron-Cetty template. Considering uncertainties of the templates, we take their mean values of $V_{\text{Fe}} = (4187 \pm 164, 3793 \pm 130) \text{ km s}^{-1}$, and find $V_{\text{Fe}} = (0.95, 0.91)V_{\text{H}\beta}$ for NGC 4593 and Mrk 1511, respectively. Interestingly, Eq. (10) roughly holds for the two objects.

Measurements of Fe II line reverberations in AGNs are a well-known hard job, but the above brief discussion of Eq. (10) predicts promising AGN candidates. As an useful criterion, relative broadness of Fe II to the H β line helps for future target campaigns of SEAMBHs to reveal Fe II physics of super-Eddington accreting AGNs.

2.8 Contamination of Fe II to H β line. We obtained the 5100 Å continuum and H β LCs using a direct integration method. The Fe II emission within the continuum and H β measurement windows, specifically the portions that cannot be removed by the integration method, may slightly influence the continuum and H β LCs. To estimate the contribution from the residual Fe II emission in the measurement windows of the integration method, we performed multi-component spectral fitting on the mean spectrum of PHL 1092. The components employed in the fitting include: (1) a power

law to model the continuum, (2) two Gaussians to model the $H\beta$ emission line, (3) a template from Boroson & Green (1992) to model the Fe II emission, and (4) a Gaussian for each of the coronal lines ([Fe VII] $\lambda\lambda 5158, 5176$ and [Ca V] $\lambda 5309$, as described by Ref.¹⁰¹).

From the fitting results (see Fig. 8), we found that the integration method may indeed retain some Fe II contribution in the continuum and $H\beta$ windows, however, these fractions are small. The Fe II residual contributes only 11% in the continuum window and 6% in the $H\beta$ window. Given that the Fe II variability during the campaign is estimated to be approximately 3-4% (as seen in the Fe II LC), which is even smaller than the variation amplitude of the continuum and $H\beta$, the impact of the Fe II residuals on the continuum and $H\beta$ LCs can be considered negligible.

2.9 Contamination of diffusive continuum. There is growing evidence for continuum contamination contributed by the diffusive continuum risen by the BLRs, even up to 23% on average in the sample¹⁰³. We note that this number is based on several important assumptions, such as, the lags of diffusive continuum is half of the $H\beta$ and the BLR covering factor is 20%, as in Ref.¹⁰⁴, or even 50% in Ref.¹⁰⁵. In the sample of Ref.¹⁰³, the averaged $EW(H\beta)$ is about 70-80 Å (similar to normal quasars), while PHL 1092 is a weak-line quasar and $EW(H\beta) \approx 40$ Å. Therefore the diffusive continuum in this object should be significantly smaller than the averaged values of AGN sample¹⁰³ in light of the smaller covering factor. Actually, the roles of the diffusive continuum are always forcing the lags toward zero. Therefore, the current leading delays cannot be resulted from the diffusive continuum, in particular, PHL 1092 is a weak-line quasar.

3 Lag measurements

The interpolated cross-correlation function (ICCF)¹⁰⁶ is widely employed to obtain $H\beta$ lags, but it is based on linear interpolations. The ICCF method often generates small multiple peaks due to noises of data, and it gets worse when there are season gaps in long term campaigns. It has been demonstrated that interpolations based on statistically and observationally motivated models are

more reliable than the ICCF^{107,108}, such as JAVELIN¹⁰⁹ and MICA[‡] (Multiple and Inhomogeneous Component Analysis¹¹⁰), and thus generate reasonable lags. Both JAVELIN and MICA employ a damped random walk (DRW) model to characterize the continuum LC but they make use of a top-hat transfer function and a transfer function composed of a sum of Gaussians, respectively. In this work, we adopt a single Gaussian in MICA. Hence, the delays are determined by the center of the Gaussian function, while their corresponding uncertainties are estimated using the 15.87% and 84.13% quantiles derived from the posterior samples generated by the Markov Chain Monte Carlo (MCMC) method.

As shown in Fig. 2, the H β LCs are fit well by the DRW model except for two epochs (MJD-58000 +800 and +2500). These could be caused by the non-concordant reverberations if composite responses to the spatially inhomogeneous variations of the extended continuum sources (see § 4). In order to avoid this complexity, we separate the LCs into three parts for determinations of reverberation delays as shown in panels **b, c, d** of Fig. 2. Generally, the DRW models fit the LCs of different periods quite good. All the separate parts and the entire LCs demonstrate that H β line variations are leading the 5100 Å, namely, the leading delays of the H β line reverberations.

Additionally, we also provide measurements of the H β lags with respect to the broad-band photometry LCs in Fig. 9. The mean lags are -12.0 , -7.8 , -31.2 , -18.0 days for the same periods with that of Fig. 2, respectively. We note some slight differences between the results from the photometry. These are caused by the fact that the photometry covers some contributions of emission lines. The consistent results also provide robustness of the LDRs in PHL 1092.

4 A toy model for anomalous reverberations

In order to understand the LDRs, we build up a toy model to illustrate the reverberations under spatially inhomogeneous variations of ionizing sources and the 5100 Å continuum. Considering

[‡]<https://github.com/LiyAstroph/MICA2>

a central ‘lamp-post’ generating X-ray variations $L_X(t)$ as shown in Fig. 4, we have the ionizing flux as responses to these variations as described by Eq. (25). Ionizing and the 5100 Å sources are simplified as two rings radii R_{ion} and R_{5100} , respectively, distributing over the rings. Subsequently it drives the variation in the emission line as Eq. (26), the variations at 5100 Å also align with the ‘lamp-post’ as indicated by Eq. (24).

In our simulations, the X-ray variation $L_X(t)$ is modeled as a damped random walk with a timescale of $\tau_d = \tau_X = 150$ days and an amplitude of $\sigma_d = \sigma_X = 0.25$ in Eq. (19). As the simplest configuration, N_* ionizing sources are distributed along a ring with a radius of R_{ion} . The flux from each source can be expressed as follows:

$$L_{\text{ion},i}(t) = L_X(t - t_{\text{ion}}); \quad \text{and } t_{\text{ion}} = (1 - \cos \phi_i \sin i_o) \left(\frac{R_{\text{ion}}}{c} \right), \quad (11)$$

where ϕ_i represents the azimuthal angle of the i -th source, and i_o denotes the inclination angle of the observer. We take $i_o = 30^\circ$ for all the cases. The clouds in the BLR will respond to the variations of each ionizing source independently, as given by:

$$L_{\text{H}\beta,i}(t) = \int_0^\infty d\tau L_{\text{ion},i}(t - \tau) \Psi_i(\tau), \quad (12)$$

where $L_{\text{H}\beta,i}$ represents the variation in line emission caused by the i -th component of the ionizing source, and Ψ_i is the corresponding transfer function. Given the responsivity distribution $g(\mathbf{r})$ of the BLR, the transfer function can be calculated as follows:

$$\Psi_i(\tau) = \int d^3r \frac{g(\mathbf{r})}{|\mathbf{r} - \mathbf{r}_i|^2} \delta[\tau - |\mathbf{r} - \mathbf{r}_i| + (\mathbf{r} - \mathbf{r}_i) \cdot \hat{\mathbf{n}}], \quad (13)$$

where \mathbf{r}_i denotes the position of the i -th source, and $\hat{\mathbf{n}} = (\sin i_o, 0, \cos i_o)$ is the unit vector pointing from the source to the observer. For simplicity, we assume that the BLR forms a uniform ring with a radius of R_{BLR} . Consequently, we have

$$\Psi_i(\tau) = \int_0^{2\pi} d\phi \frac{\delta(\tau - \tau_i)}{\Delta_i^2}, \quad (14)$$

where

$$\Delta_i = \sqrt{(R_{\text{BLR}} \cos \phi - R_{\text{ion}} \cos \phi_i)^2 + (R_{\text{BLR}} \sin \phi - R_{\text{ion}} \sin \phi_i)^2} \quad (15)$$

and

$$\tau_i = \left(\frac{1}{c}\right) [\Delta_i - (R_{\text{BLR}} \cos \phi - R_{\text{ion}} \cos \phi_i) \sin i_o]. \quad (16)$$

The number and azimuthal angles of the 5100 Å sources are identical to those of the ionizing sources. Consequently, the continuum from the i -th source is

$$L_{5100,i}(t) = L_X(t - t_{5100}); \quad \text{and } t_{5100} = (1 - \cos \phi_i \sin i_o) \left(\frac{R_{5100}}{c}\right). \quad (17)$$

The observed LCs of the 5100 Å continuum and H β line are then

$$L_{5100}(t) = \sum_{i=1}^{N_*} L_{5100,i}(t) \quad \text{and} \quad L_{\text{H}\beta}(t) = \sum_{i=1}^{N_*} L_{\text{H}\beta,i}(t), \quad (18)$$

respectively. Given the parameters of R_{ion} , R_{5100} and $R_{\text{H}\beta}$ of simplified model, we can simulate the observed reverberations.

Fig. 10 – 13 present results for various values of R_{ion} , R_{5100} , and $R_{\text{H}\beta}$, revealing diverse non-concordance reverberations of composite responses. In general, the BLRs exhibit leading delays of reverberations with respect to the 5100 Å provided $R_{\text{H}\beta} < R_{5100}$, otherwise normal delayed reverberations occur. Emission lines correlate strongly with the continuum's large-scale structures over extended timescales but show poor responsiveness to small-scale structures—especially with multiple ionizing sources. Shaded areas mark periods of this poor responsiveness to illustrate the effect. When BLR lies within the 5100 Å region, the line variations precede those in the 5100 Å continuum, and vice versa. The time delay between the two LCs depends on the difference in their respective sizes. Amid such complex situation of extended and inhomogeneous ionizing sources, composite-response reverberations appear non-concordant, with weak or over-responses in some periods. This non-concordant relation arises not from reprocessing physics but from differential lags caused by spatially inhomogeneous variations. Furthermore, measured lags reflect distances between the BLR and ionizing sources (not the central SMBH), invalidating the conventional SMBH mass formulation.

To better compare with observations, we resampled the mock LCs in the left panel of Fig. 14,

with an average 6-day cadence and approximately 160-day season gaps. Additionally, the observational errors for the continuum spectrum and emission lines are 1% and 3%, respectively. Fig. 14 right panel shows negative lags, which are consistent with observed anomalous reverberations. These simulations explain the aforementioned anomalies in NGC 5548, Mrk 817, and NGC 7469, as well as PHL 1092’s over-responses around MJD 58000 +800 and under-responses at +2500. Future work will use a more realistic BLR model for inhomogeneous variations to explore anomalous reverberations of the broad $H\beta$ line, with detailed results to follow.

It should be noted that in these simulations r_{\max} is significantly higher than the observational data. This is because the simulated data are generated under ideal conditions — no random fluctuations are added, leading to $r_{\max} \sim 0.9$ (Figs. 10–13). Additionally, the three components (ionizing sources, BLR, and 5100 Å regions) are simplified as rings with different radii. Recognizing this, more realistic models are needed to simulate PHL 1092’s observations.

5 Aliasing effects

To investigate whether the aliasing effect can result in a leading lag due to seasonal gaps, sampling, and scatters in the LCs from the current RM observations, we conducted a series of Monte Carlo simulations with the following steps. First, we fit the observed LCs of PHL 1092 through the DRW model to obtain two parameters of timescales and amplitudes describing variations, namely,

$$S_{ij} = \sigma_d^2 \exp\left(-\frac{|t_i - t_j|}{\tau_d}\right), \quad (19)$$

where t_i and t_j are the time of two points in the continuum LCs, σ_d is the variation amplitude at long timescale, τ_d is the characteristic damped timescale. We determine the two parameters by fitting the observed whole continuum LC using MCMC method. We obtain $\sigma_d = 1.42 \times 10^{-3}$ (in arbitrary units) and $\tau_d = 267$ days, where these values represent the median estimates derived from the posterior distribution of the MCMC samples. Using these parameter values, we generate mock LCs of the continuum with daily sampling. Second, we make use of the Gaussian function as the

BLR transfer function

$$\Psi_{\text{BLR}}(t) = \frac{1}{\sqrt{2\pi}\Delta\tau_0} \exp\left[-\left(\frac{t - \tau_{\text{H}\beta}}{\Delta\tau_0}\right)^2\right], \quad (20)$$

to obtain H β LCs, where $\Delta\tau_0$ is the width of the function. We take $\tau_{\text{H}\beta} = 16$ days (corresponding to the lag predicted by the new scaling relation⁷) and a standard deviation of 5 days (equal to one-third of the lag), $\Delta\tau_0 \approx \tau_{\text{H}\beta}/3$, which means that $\tau_{\text{H}\beta} - 3\Delta\tau_0 = 0$ appears as zero-lag reverberation. Actually, this is a conservative estimation, for example, $\Delta\tau_0 = 0.1\tau_{\text{H}\beta}$ in Ref.¹¹¹ and $\Delta\tau_0 = 0.2\tau_{\text{H}\beta}$ in Ref.¹¹² for mock LCs of reverberations. Moreover, we also tested how the results of the simulations depend on the input width of the Gaussian functions. We find that results from $\Delta\tau_0 = 10$ days are very similar to that of $\Delta\tau_0 = 5$ days. In practice, MICA and JAVELIN based on physical model for interpolations are a powerful tool to determine the lags, generating results very insensitive to the width of the transfer functions. Subsequently, the two LCs are linearly interpolated onto the corresponding observed epochs to mimic real observations. To enhance the realism of the mock LCs, Gaussian noise is systematically introduced, ensuring that the relative errors are consistent with those observed in the actual data. Finally, we measured the lags of the mock continuum and emission-line LCs using MICA with the same settings applied to the measurements of the actual LCs of PHL 1092.

We repeat the above procedure 5000-20000 times. Fig. 15 shows simulation results, yielding probabilities of random LDRs from aliasing effects and error bars listed in Tab. 2. We found that the probability of getting a leading lag with $\tau_{\text{MICA}} < -16$ days is 5×10^{-5} based on the lag distribution from the mock data for the whole length of the campaign. The significance of other periods is also close to 4σ listed in Tab. 2. We therefore conclude that the LDR detection is significant at a level of 4.0σ in PHL 1092.

Finally, we plot residuals of the fittings in Fig. 6. The residual distributions are approximately Gaussian, indicating that the tests of aliasing effects are robust. The observed LDRs in PHL 1092 are intrinsic phenomena.

6 Standard model of accretion disks

Considering potential configurations of the PSA invalidity, we have to examine sizes of accretion disks which play a key role in the reverberation physics, in particular, when the sizes are comparable to the BLRs. For the regime of $0.1 \lesssim \dot{\mathcal{M}} \lesssim 3$, the Shakura-Sunyaev model usually assumes a Keplerian rotation around the central SMBH with α -viscosity description, and that the radial motion velocity of accreting gas is much smaller than the rotation velocity, enabling the local energy balance³⁰. Additionally, the disk is cold (relative to local virial temperatures) because dissipated energy is radiated away locally and instantaneously. The energy dissipation rate per unit area of the disk is given by^{30,113},

$$Q_{\text{vis}} = \frac{3}{8\pi} \frac{GM_{\bullet}\dot{M}_{\bullet}}{R^3} = 6.86 \times 10^{10} \dot{\mathcal{M}} M_7^{-1} r_3^{-3} \text{ erg cm}^{-2} \text{ s}^{-1}, \quad (21)$$

where $r_3 = R/10^3 R_g$, the boundary factor is neglected for $R/R_g \gg 1$. We would emphasize that this rate is fully independent of any viscosity. The effective temperature of the disk surface approximately treated as a black body is given by $\sigma_{\text{SB}} T_{\text{eff}}^4 = Q_{\text{vis}}$, namely

$$T_{\text{eff}} = 5.89 \times 10^3 \dot{\mathcal{M}}^{1/4} M_7^{-1/4} r_3^{-3/4} \text{ K}. \quad (22)$$

Since the Planck function can be well approximated by the δ -function of wavelength (see Eq. 4.39 in Ref.¹¹⁴), we have the radius of emitting ϵ photons from the Wien's law,

$$\frac{R_{\epsilon}}{R_g} = 4.9 \times 10^2 (\epsilon/\epsilon_{5100})^{-4/3} \dot{\mathcal{M}}^{1/3} M_7^{-1/3}, \quad (23)$$

showing that R_{ϵ} increases with accretion rates, where $\epsilon_{5100} \approx 2.2 \text{ eV}$ is photon energies at 5100 \AA . For $\epsilon = \epsilon_{5100}$ and a typical SMBH-disk with $\dot{\mathcal{M}} = 1$ and $M_7 = 1$, we have $R_{5100} \approx 500 R_g \ll R_{\text{BLR}}$ (Eq. 2a), indicating validity of the PSA when accretion rates are not much super-Eddington ($\dot{\mathcal{M}} \lesssim 10^2$). Therefore Eq. (3) generally applies to most low- \mathcal{R}_{Fe} AGNs.

Isotropy of emissions from slim disks has been examined²⁸ showing anisotropy of the ionizing energy source for $\dot{\mathcal{M}} \gtrsim 10$ accretion disks. The anisotropy of Shakura-Sunyaev disk³⁰ can

be approximated by $\cos i$, and hence as roughly isotropic sources if they are face-on. Whatever accretion rates of slim disks, the self-obscurations of slim disks cannot lead to the LDRs.

7 Challenging questions

The LDRs of PHL 1092 raise a series of fundamental questions listed below, which pertain to the inner structure of AGNs, in particular, the extra energy sources beyond the SMBH-disk could be involved. We discuss these questions with speculative insights, grounded in observational evidence.

First, with the PSA invalid, how to estimate SMBH masses for PHL 1092 analogs remains open since Eq. (3) is no longer valid. In such a context, only order estimations of SMBH masses can be made. In § 8, we provide some analytical discussions on transfer functions between the $H\beta$ and 5100 Å LCs for SMBH masses. In order to simply illustrate, we consider the BLR simplified as a ring. If neglecting the spatial extension of the 5100 Å regions, the width of the transfer function is given by $2R_{\text{ring}} \sin i/c$, where R_{ring} is the ring radius. See details in Fig. 19 of page 114 in Ref.¹¹⁴. Therefore, R_{ring}/c from the transfer function can be regarded as the rough width of the BLRs for SMBH masses. In practice, using the transfer function for M_{\bullet} could be a quite reliable approximation when the reverberations are anomalous. Transfer functions of the BLRs, which are obtained by JAVELIN and MICA measurements through fitting the continuum and $H\beta$ LCs, yield the full-width half maximum of the BLRs (ΔR_{min}). The BLR size can be approximated by ΔR_{min} to replace $R_{H\beta}$ in Eq. (3) for SMBH masses. For PHL 1092, we have $R_{H\beta} \approx \Delta R_{\text{min}} \approx 25$ ltd from MICA analysis of the whole LC (see Fig. 2 in § 3 and related discussions in § 8). We have $M_{\bullet} = 2.5 \times 10^7 M_{\odot}$ and accretion rates of $\dot{M} \approx 200$, suggesting that this is a super-Eddington accreting AGN.

Modeling the BLR reverberations through MCMC simulations is a powerful method of accurately measuring SMBH masses^{115,116}, however, the method is not valid for the extremely anomalous reverberations (the PSA is invalid) because the 5100 Å region and BLR sizes are degenerate,

and the 5100 Å sizes as a reference to the central SMBH distances is entirely unknown. Fortunately, GRAVITY/VLTI measurement based on spectroastrometry¹¹⁷ would be a key to measure SMBH masses since it models profiles of the broad emission line and its differential phase curve whatever the SMBH-disk sizes are. If the SARM (SpectroAstrometry and Reverberation Mapping)¹¹⁸ analysis is employed, the SMBH masses and disk sizes are expected to be generated simultaneously. This may allow us to determine spatial distributions of sMBHs over the s@SMBH-disk.

If the spatial inhomogeneity scale is comparable to the radius of the s@SMBH-disk ($\Delta R \sim R$, see Issue 6 in § 7 below), the approximation of a monotonic temperature-radius ($T - R$) relation breaks down. This will open a new research direction for high spatial resolution astronomy with future kilometer-baseline interferometers⁶⁰. The measured masses will encompass all components within the spatially resolved radius (including gaseous mass, sMBHs, and the central SMBH). The pure mass of the central SMBH must be inferred from the detailed fine structure of differential phase curves though this remains uncertain in current GRAVITY observations¹¹⁷.

Second, what mechanism governs the shortening of $H\beta$ reverberation lags and the emergence of LDRs? We define a parameter of $\delta\tau = \tau_{H\beta}/\tau_{H\beta}^0$, this parameter ranges approximately from $[-50, 1]$ from PHL 1092. While delay shortening of SEAMBHs can be partially explained in some degrees by the self-obscuration of the inner part of slim disks²⁸, this cannot account for the LDRs (i.e., $\delta\tau \leq 0$). Fig. 3 shows the large gap between the $R_{H\beta} = -(17 \sim 57) \text{ ltd}$ and the $R_{H\beta} - (L, \mathcal{R}_{Fe})$ relation, but there is growing evidence for analogs with anomalous reverberations (see a brief discussion in Issue 3 in § 7) filling the gap. If the transition from shortened lags to LDRs is continuous, the shortening mechanism is likely not pure self-obscuration but other processes, e.g., EESs stretching the SMBH-disk system depending on the number of embedded stellar-mass black holes (sMBHs). AGN disks are estimated to contain $\sim 10^3 - 10^5$ massive stars¹¹⁹ over AGN episodic lifetimes, these stars can evolve into sMBHs (with approximately same number $\sim N_\bullet$) and Fe elements¹²⁰. In the simplest version, a relation of $\mathcal{R}_{Fe} \propto N_\bullet$ is expected (of course, it is still controversial^{121, 122} if \mathcal{R}_{Fe} can be used for exact metallicity¹²³ since it is also sensitive to ionized

gas density, temperatures and turbulence). Therefore, the structures of high- \mathcal{R}_{Fe} AGNs controlled by the EESs can be tested by RM campaigns of broad emission lines of the BLR and continuum of accretion disks, or by micro-lensing effects for measurements of the SMBH-disk sizes^{124–126}.

Third, what are occurrence rates of the LDRs in AGNs analogous to PHL 1092? It is still too early to provide a definitive answer. Our campaigns have monitored ~ 20 targets for over 7 years. Among these, several show severely shortened $\text{H}\beta$ lags — $\tau_{\text{H}\beta}$ approaches zero or becomes negative (shortening factors exceed 10), and some (e.g., SDSS J224028-10649) even oscillate between positive and negative lags across epochs. Examples include Mrk 1239[§], PG 0043+039, PG 1244+026, PG 1543+489, PHL 1811 (a weak-line quasar) and SDSS J224028-10649. We have $\sim 25\%$ of our total sample appearing anomalous reverberation but the sample is heterogeneous. These objects violate the PSA and may be PHL 1092 analogs, but their more complex delay behaviors suggest more intricate inner structures. We will report these objects separately once their properties are definitive. However, they lack distinct single-epoch spectral features to differentiate them from PHL 1092, making it impossible to pre-select the analogs. To address this question, long-term, high-cadence RM campaigns of more high- \mathcal{R}_{Fe} AGNs are needed to systematically search for such LDRs. Except for the LDRs in this paper, the long-standing unresolved issues of $\text{H}\beta$ reverberation trending in some AGNs⁹⁹ could be also driven by the SMBHs.

Additionally, some targets have variation amplitudes too small to measure lags—even over several years. These objects typically have high- \mathcal{R}_{Fe} and may resemble the so-called "extremely stable quasars"¹²⁹, which is notable. Systematically investigating the temporal properties of AGNs as a function of \mathcal{R}_{Fe} is undoubtedly crucial.

Fourth, how many SMBHs are in an SMBH-disk if EESs are powered by them? A key clue to this question is why AGN BLRs are so metal-rich (i.e., high- Z). Previous work^{120,130–133}

[§]see its complex spectra¹²⁷; the first 3-year of our RM campaign showed no anomalies¹²⁸, but latest 3-year data exhibit anti-reverberation in our six-year campaign.

suggests BLR metals form via star formation in nuclear regions, and SMBHs as remnants of massive stars their numbers should correlate with BLR metallicity. Thus, \mathcal{R}_{Fe} as a proxy of BLR metallicity¹²³ might also indicate numbers of SMBHs, which control the $R_{\text{H}\beta} - (L, \mathcal{R}_{\text{Fe}})$ relation of the SEAMBHs⁷. However, it is not a straightforward job to theoretically derive this relation, which involves evolution of massive stars formed from fast accretion^{120,134}. About $10^3 - 10^5$ SMBHs are estimated in SMBH-disk¹¹⁹. Additionally, while AGN structures comprise accretion disks, BLRs, and dusty tori, their formation mechanism has remained unresolved since quasars were first discovered. A critical question arises: if SMBHs are sufficiently abundant, can they play important roles in AGN structure and evolution? Clearly, establishing relationships between \mathcal{R}_{Fe} , metallicity (Z), and SMBH number (N_{\bullet}) — as well as linking these to the $R_{\text{H}\beta} - (L, \mathcal{R}_{\text{Fe}})$ relation—will be a pivotal future task.

Fifth, what are the temporal properties of the s@SMBH-disk? This question prompts us to recall that X-ray binaries exhibit quasi-periodic oscillations (QPOs) across various frequencies^{135,136}. By contrast, AGN QPOs are extremely rare except for a few objects, such as X-ray QPOs in RE J1034+396¹³⁷. This implies AGN SMBH-disk systems are not simply black hole mass-scaled versions of X-ray binary accretion disks. A heuristic hypothesis is that the difference stems from the presence of s@SMBH-disk in AGNs. In this scenario, SMBHs suppress gaseous oscillations in the SMBH-disk. For instance, a kind of QPOs with a frequency of $\nu \sim c_s/H$ will be destructed by the Bondi accretion of SMBHs with a timescale of R_{Bon}/c_s , where c_s is the sound speed, R_{Bon} is the Bondi radius and $R_{\text{Bon}} \sim H$. Nevertheless, SMBHs play a key role in AGN variability.

Moreover, Eq. (1) shows that if $Q_{\text{extra}} \gtrsim Q_{\text{vis}}$, the effective temperature distribution is drastically modified, producing warm outer regions of the SMBH-disk, namely, $R_{5100}^{\bullet} \gg R_{5100}$, where R_{5100}^{\bullet} is the 5100 Å radius of the s@SMBH-disk. This leads to that the reprocessed emissions appear far more temporally stable (longer variability timescales but much smaller amplitudes than normal AGNs). This could explain why SEAMBH LCs are typically more stable than those of sub-Eddington AGNs¹³⁸, assuming the SMBH-disk of SEAMBHs contain more SMBHs than the

sub-Eddington (which are usually low- \mathcal{R}_{Fe} objects. Emissions from sMBHs dominate the SMBH-disk so that they share high stability since the total variations are smeared by the widely spatial distribution of sMBHs across the disk). Notably, extremely stable quasars have recently been identified¹²⁹ — these may be more extreme cases than PHL 1092. A correlation between F_{var} and \mathcal{R}_{Fe} should be explored in a large sample, and investigating sMBH roles in AGN variability across multiwavelengths is highly prioritized.

Furthermore, growing evidence from microlensing indicates accretion disk sizes are significantly larger than standard model predictions^{125, 126}. Approximately ten AGNs have been jointly observed by *Swift* and ground-based telescopes to constrain disk sizes. The measured lags are $\sim 2 - 3$ times those of the standard accretion disk model^{34, 103, 107, 139}. This substantial discrepancy could be explained by modified black-body radiation from the disk surface, driven by the disk's detailed vertical structure¹⁴⁰. However, s@SMBH-disk will exhibit distinct behavior in multi-color reverberations of the SMBH-disks, in particular, will show lags far longer than standard accretion disks. Indeed, Mrk 335 has a $\sim 8000 \text{ \AA}$ continuum size ten times larger than the standard model prediction¹⁴¹. Future reverberation mapping of accretion disks in PHL 1092 analogs will measure these stretched disks; the powerful Vera Rubin Telescope (LSST), in particular, will enable systematic accretion disk size measurements for a large AGN sample.

Additionally, sMBH roles in variability remain unclear, except for their involvement in outbursts via the Bondi explosions^{41, 142}. Under the lamp-post model, reprocessing follows X-ray variations, but variability timescales are determined by light-crossing times of the s@SMBH-disk. However, the spread of UV and optical continuum variations reduces amplitudes, making it harder to measure delays of continuum reverberations via multi-wavelength campaigns.

Sixth, how do sMBHs migrate toward the central SMBH? Studies of sMBH populations^{143–145} show: (1) migration timescales depend on SMBH-disk accretion rates; (2) more massive sMBHs migrate inward faster than less massive ones; (3) hierarchical sMBH mergers^{51, 52, 146} drive the

growth of recently observed $\sim 100 M_{\odot}$ sMBHs^{47,48}, even forming multi-body systems of several massive black holes in nuclear central regions; (4) multi-scattering of sMBHs with gaseous drag can form sMBH clusters inside/outside the SMBH-disk, causing spatial inhomogeneity in ionizing components (observationally referred to as hot spots). This dynamical behavior, in principle, produces an interesting consequence of AGN temporal properties. AGNs with higher accretion rates rapidly swallow sMBHs, gradually evolving into sub-Eddington AGNs with fewer, intermediate/massive black holes. In sub-Eddington AGNs, sMBHs play a minor role in SMBH-disk heating ($R_{5100}^{\bullet} \approx R_{5100} \ll R_{H\beta}$) but can trigger strong AGN variability (e.g., outbursts^{41,142,147}). By contrast, s@SMBH-disk contains more sMBHs — enabling efficient heating and producing structures with $R_{5100}^{\bullet} < R_{5100}$, $R_{5100}^{\bullet} \sim R_{H\beta}$ (zero-lag reverberations), or even $R_{5100}^{\bullet} > R_{H\beta}$ (leading delay of responses, LDRs). SEAMBH-focused campaigns are expected to detect all such anomalous reverberations, helping establish the potential sequence of dynamical evolution of sMBHs.

The existence of intermediate BHs around the central SMBH may drive a type I migration making the inner part of the SMBH-disk unstable. This may yield the increasingly interesting phenomena of changing-look AGNs¹⁴⁸ through interaction of massive black holes with companion's disk¹⁴⁹, which are showing increasingly more complicated behaviors¹⁵⁰. It is also possible that successive mergers of sMBHs to form a few bodies of SMBHs, and even leave a binary-SMBH in galactic centers. Except for galaxy mergers, this is a new way to form binary SMBHs in galaxies radiating nano-Hz GWs expected by PTA detections^{151–153}. Individual identifications of binary-SMBHs can be done by RM campaigns^{154–157} or spatially resolved by optical interferometers, such as GRAVITY/VLTI^{158,159}.

Seventh, non-concordant reverberations as the effects of the spatially inhomogeneous variations (incoherent in time and amplitudes) of an extended ionizing source have been discovered from simple Monte Carlo simulations in § 4. This applies to PHL 1092, which shows weak responses (anomalous behavior) at a few epochs. When $R_{5100} \gtrsim R_{H\beta}$ holds, the LDRs emerge, and non-concordant responses become more complex — this lies beyond the classical RM framework (see

fundamental assumptions in Ref.²). More realistic models are therefore needed to explain such anomalous reverberations.

Observationally, the LDRs in PHL 1092 are the first extreme outliers from the known $R_{\text{H}\beta} - (L, \mathcal{R}_{\text{Fe}})$ relation. Future campaigns require the highest possible cadence to probe ionizing source inhomogeneities in PHL 1092, in particular, 6–8 m telescopes are necessary for high-fidelity RM improving spectral calibration and addressing annual scatter in spectroscopic data. While § 4 only explores ionizing source inhomogeneities and inhomogeneous BLRs cloud distributions are also plausible, both inhomogeneities could be detected by future high-fidelity campaigns. Non-concordant reverberation effects will then help unravel the complex structures and components around the central SMBH. However, annual lags may vary, as ionizing source components are random and varying somehow. These random lag values reflect inhomogeneity of the ionizing sources and their non-synchronized variabilities — potentially explaining the multiple $\text{H}\beta$ reverberation lags noted in Issue 3 of § 7 for our sample.

In summary, LDRs pose significant challenges to the standard AGN model. As briefly discussed in § 9, SMBHs accreting within the SMBH-disk can provide additional energy sources and act as a new mechanism governing extremely anomalous $\text{H}\beta$ reverberations (e.g., PHL 1092 as reported here). This may represent just the tip of the iceberg in AGNs hosting s@SMBH-disk.

8 Reverberations of the lamp-post model

JAVELIN and MICA don’t make use of the PSA, but we illustrate the physical implications of the transfer functions. In the lamp-post model, the 5100 Å, ionizing photon and $\text{H}\beta$ fluxes are related to the X-ray flux as

$$L_{5100}(t) = \int \Psi_{5100}(\tau) L_X(t - \tau) d\tau, \quad (24)$$

$$L_{\text{ion}}(t) = \int \Psi_{\text{ion}}(\tau) L_X(t - \tau) d\tau, \quad (25)$$

and

$$L_{\text{H}\beta}(t) = \int \Psi_{\text{H}\beta}(\tau) L_{\text{ion}}(t - \tau) d\tau, \quad (26)$$

where Ψ are transfer functions of the 5100 Å, ionizing sources and H β regions. Inserting Eq. (25) into (26), we have

$$L_{\text{H}\beta}(t) = \int d\tau \Psi_{\text{H}\beta}(\tau) \int d\tau' \Psi_{\text{ion}}(\tau') L_X(t - \tau - \tau'). \quad (27)$$

In the stretched SMBH-disk, $\Psi_{\text{ion}}(\tau) \approx \delta(\tau - \tau_0)$ is still valid by δ function (ionizing source is a narrow ring) in the face-on case, we have

$$L_{\text{H}\beta}(t) = \int \Psi_{\text{H}\beta}(\tau - \tau_0) L_X(t - \tau) d\tau. \quad (28)$$

By performing a Fourier transformation to Eqs.(24) and (28), we have

$$\mathcal{F}[L_{\text{H}\beta}(t)] = \frac{\mathcal{F}[\Psi_{\text{H}\beta}(\tau - \tau_0)]}{\mathcal{F}[\Psi_{5100}(\tau)]} \times \mathcal{F}[L_{5100}(t)], \quad (29)$$

where \mathcal{F} denotes the Fourier transformation. Eq.(29) corresponds to a convolution in the time domain as

$$L_{\text{H}\beta}(t) = \int \Psi_R(\tau) L_{5100}(t - \tau) d\tau, \quad (30)$$

where

$$\Psi_R(\tau) = \mathcal{F}^{-1} \left[\frac{\mathcal{F}[\Psi_{\text{H}\beta}(\tau - \tau_0)]}{\mathcal{F}[\Psi_{5100}(\tau)]} \right]. \quad (31)$$

The current analysis of JAVELIN and MICA is equivalent to solving Eq. (30). The obtained transfer functions therefore represent an approximation to $\Psi_R(\tau)$.

In cases of $R_{5100} \ll R_{\text{H}\beta}$, it is safe to approximate $\Psi_{5100}(\tau) \approx \delta(\tau - \tau_{5100})$, where τ_1 is the delay with respect to the X-ray source. Then Eq. (31) will be simplified to $\Psi_R(\tau) = \Psi_{\text{H}\beta}(\tau - \tau_0 + \tau_{5100})$. In cases of $R_{5100} \sim R_{\text{H}\beta}$, $\Psi_{5100}(\tau)$ cannot be simply treated as a δ function. If we approximate $\Psi_{\text{H}\beta}(\tau)$ and $\Psi_{5100}(\tau)$ as Gaussians with the respective center $\tau_{\text{H}\beta}$ and τ_{5100} and the respective standard deviation $\sigma_{\text{H}\beta}$ and σ_{5100} , Eq. (31) illustrates that $\Psi_R(\tau)$ is also a Gaussian. The Gaussian center is equal to $\tau_R = \tau_{\text{H}\beta} + \tau_0 - \tau_{5100}$ and the Gaussian standard deviation is equal to $\sigma_R = (\sigma_{\text{H}\beta}^2 - \sigma_{5100}^2)^{1/2}$. In practice, $\Psi_{\text{H}\beta}(\tau)$ and $\Psi_{5100}(\tau)$ might exhibit more complicated shapes, rather than following a

simple Gaussian profile. However, it remains valid that the time lags measured by JAVELIN and MICA analysis on the $H\beta$ and 5100 \AA LCs can be approximately regarded as the difference between $\tau_{H\beta} + \tau_0$ and τ_{5100} , which typically represent the sizes of the $H\beta$ and 5100 \AA regions, respectively. In other words, the measured time lags reflect the size difference and a negative $H\beta$ time lag with respect to 5100 \AA means that the $H\beta$ region is located inside the 5100 \AA regions.

We note that discussions presented here remain in an analytical form and our simulations in § 4 are also for characterized models. Realistic models of BLRs and accretion disks for the transfer functions along with a toy model of the anomalous reverberations will be considered for PHL 1092 in an separate paper.

9 Discussions on potential models

The negative lags set strong constraints on the configurations of the BLR and SMBH-disk. There are several potential models listed below and we briefly comment on them. Based on the subsequent discussions, we would draw a conclusion that the leading delays are plausibly driven by stretching SMBH-disk through SMBHs heating.

3D geometry of disk. We made efforts to explain the shortening of $H\beta$ lags in super-Eddington AGNs, where the inner funnel of slim disks makes anisotropic radiation toward BLR clouds and observers²⁸. This effect can account for a shortening factor of $\sim 10^{-0.35R_{Fe}} \lesssim 5$, however, cannot generate the negative lags observed in PHL 1092 unless the BLR clouds are predominantly located in the pole regions. This model is therefore disfavored for explaining leading delays.

An outflowing BLR over the disk. Outflowing BLRs parallel to the disk surface have been extensively studied¹⁶⁰, assuming the ionizing regions of accretion disks are point-like. While lags in this scenario are complex, no leading delays have been found in their simulations in any case. The LDRs necessarily require an extended ionizing source. Additionally, pole-dominated winds can produce leading reverberation delays, but extended ionizing sources larger than the cross-sectional

radius of the outflowing BLRs are still necessary.

Anomalous viscosity in accretion disk. In fact, the energy dissipation rate per unit area is fully independent of viscosity/turbulence physics—unless the gas has non-Keplerian rotation. This was elegantly demonstrated by Lynden-Bell¹¹³ and is also covered in standard textbooks¹⁶¹. By contrast, radiation from slim disks¹⁶² depends on viscosity, as these disks are sub-Keplerian. To generate LDRs, viscosity would need to be modified into a complex form producing non-monotonic effective temperature distributions in the disk's outer regions (e.g., a double power-law with respect to disk radius). However, such an unusual viscosity profile requires specific physical mechanisms. Again, s@SMBH-disk may fulfill this role in LDR formation.

Extended winds from super-Eddington accretion. Recently, extended winds from super-Eddington accretion have been proposed to play a key role in explaining "little red dots"¹⁶³, producing the observed Balmer break. Intriguingly, these winds might extend to the broad line region (BLR), potentially generating the LDRs. For a simple disk wind estimate, its radius is given by $R_w/R_g = \tau_{\text{es}}\beta_w\dot{M}_w/\dot{M}_{\text{Edd}}$ from an approximate spherical wind model: $\dot{M}_w = 4\pi R_w^2 V_w \rho_w$, where $\beta_w = V_w/c$ is the wind velocity, $\tau_{\text{es}} = \rho_w \kappa_{\text{es}} R_w$ is the Thomson scattering depth of the winds, and ρ_w is wind mass density. If 5100 Å photons are scattered by these winds, $R_w \gtrsim R_{\text{H}\beta}$ is required, implying a lower limit on the central super-massive black hole (SMBH) accretion rate $\dot{\mathcal{M}} \gtrsim \dot{M}_w/\dot{M}_{\text{Edd}}$. This yields $\dot{\mathcal{M}} \gtrsim 10^3 (\tau_{\text{es}}\beta_w/0.1) (R_{\text{H}\beta}/10^4 R_g)$, indicating extremely high slim disk accretion rates are needed to produce such strong winds.

Observationally, our campaigns have identified a few super-Eddington accreting massive black holes (SEAMBHs) with potentially high rates (e.g., IRAS 04416+1215: $\dot{\mathcal{M}} = 10^{2.63}$; SDSS J084533.28+474934.5: $\dot{\mathcal{M}} = 10^{2.76}$; SDSS J100402.61+285535.3: $\dot{\mathcal{M}} = 10^{2.89}$)⁷. However, these SEAMBHs do neither exhibit absorbing features of H β nor the LDRs, and their velocity-resolved delays do not support strong outflows in SEAMBHs¹⁶⁴. Though we are not able to rule out this possibility within ranges of the parameters, this simple estimate thus disfavors slim disk winds as

the cause of LDRs. That said, the idea remains interesting and merits further qualitative exploration for both lag shortening and LDRs.

Satellite SMBHs. There is growing evidence for the presence of satellite black holes around the central SMBH. For instance, mHz quasi-periodical oscillations (QPOs) of X-ray variations in AGN 1ES 1927+654⁵³, and quasi-periodical ejections (QPEs) in galaxies of Seyfert 2 galaxy GSN 069⁵⁴ and others^{55–58}. Moreover, high metallicity of AGN BLRs indicate formation of massive stars inside the accretion disks^{120,134,165}, and compact objects from evolution of massive stars remain there⁸. The s@SMBH-disk suggested for the LDRs is generally consistent with the above evidence and arguments. sMBHs must play a role in variations of continuum and BLRs somehow^{41,142}, yielding the anomalous reverberations of broad $H\beta$ line. In such a context, GWs are expected from detections of LIGO, LISA¹¹/Tianqin¹² and ET¹³. LIGO already has observational hints from joint analyses with long-term photometric monitoring campaigns^{44–48,166,167}.

In summary, we prefer s@SMBH-disk scenario over the aforementioned models to explain LDRs. Considering that the PHL 1092 analogs are not so rare, we recognize that these alternative models as extreme configurations to explain the LDRs become slim. However, we emphasize that they require quantitative investigation in future.

References

1. Bahcall, J. N., Kozlovsky, B.-Z. & Salpeter, E. E. On the Time Dependence of Emission-Line Strengths from a Photoionized Nebula. ApJ **171**, 467 (1972).
2. Blandford, R. D. & McKee, C. F. Reverberation mapping of the emission line regions of Seyfert galaxies and quasars. ApJ **255**, 419–439 (1982).
3. Peterson, B. M. Reverberation Mapping of Active Galactic Nuclei. PASP **105**, 247 (1993).
4. Kaspi, S. et al. Reverberation Measurements for 17 Quasars and the Size-Mass-Luminosity Relations in Active Galactic Nuclei. ApJ **533**, 631–649 (2000). [astro-ph/9911476](#).

5. Peterson, B. M. Measuring the Masses of Supermassive Black Holes. Space Sci. Rev. **183**, 253–275 (2014).
6. Bentz, M. C. et al. The Low-luminosity End of the Radius-Luminosity Relationship for Active Galactic Nuclei. ApJ **767**, 149 (2013). 1303.1742.
7. Du, P. & Wang, J.-M. The Radius-Luminosity Relationship Depends on Optical Spectra in Active Galactic Nuclei. ApJ **886**, 42 (2019). 1909.06735.
8. Cheng, K. S. & Wang, J.-M. The Formation and Merger of Compact Objects in the Central Engine of Active Galactic Nuclei and Quasars: Gamma-Ray Burst and Gravitational Radiation. ApJ **521**, 502–508 (1999). astro-ph/9908228.
9. Gilbaum, S. & Stone, N. C. Feedback-dominated Accretion Flows. ApJ **928**, 191 (2022). 2107.07519.
10. Zhou, S. et al. Stellar Black Holes Can “Stretch” Supermassive Black Hole Accretion Disks. ApJ **966**, L9 (2024). 2404.07407.
11. Amaro-Seoane, P. et al. Astrophysics with the Laser Interferometer Space Antenna. Living Reviews in Relativity **26**, 2 (2023). 2203.06016.
12. Luo, J. et al. Fundamental Physics and Cosmology with TianQin. arXiv e-prints arXiv:2502.20138 (2025). 2502.20138.
13. Di Giovanni, M. Einstein Telescope and Cosmic Explorer. arXiv e-prints arXiv:2505.11033 (2025). 2505.11033.
14. Shen, Y. & Kelly, B. C. The Demographics of Broad-line Quasars in the Mass-Luminosity Plane. I. Testing FWHM-based Virial Black Hole Masses. ApJ **746**, 169 (2012). 1107.4372.

15. Vestergaard, M. & Osmer, P. S. Mass Functions of the Active Black Holes in Distant Quasars from the Large Bright Quasar Survey, the Bright Quasar Survey, and the Color-selected Sample of the SDSS Fall Equatorial Stripe. *ApJ* **699**, 800–816 (2009). 0904.3348.
16. Yang, J. et al. A SPectroscopic Survey of Biased Halos in the Reionization Era (ASPIRE): A First Look at the Rest-frame Optical Spectra of $z > 6.5$ Quasars Using JWST. *ApJ* **951**, L5 (2023). 2304.09888.
17. Matthee, J. et al. Little Red Dots: An Abundant Population of Faint Active Galactic Nuclei at $z \sim 5$ Revealed by the EIGER and FRESCO JWST Surveys. *ApJ* **963**, 129 (2024). 2306.05448.
18. Wang, J.-M., Du, P., Valls-Gabaud, D., Hu, C. & Netzer, H. Super-Eddington Accreting Massive Black Holes as Long-Lived Cosmological Standards. *Phys. Rev. Lett.* **110**, 081301 (2013). 1301.4225.
19. Du, P. et al. Supermassive Black Holes with High Accretion Rates in Active Galactic Nuclei. I. First Results from a New Reverberation Mapping Campaign. *ApJ* **782**, 45 (2014). 1310.4107.
20. Wang, J.-M. et al. Supermassive Black Holes with High Accretion Rates in Active Galactic Nuclei. II. The Most Luminous Standard Candles in the Universe. *ApJ* **793**, 108 (2014). 1408.2337.
21. Marziani, P., Sulentic, J. W., Zwitter, T., Dultzin-Hacyan, D. & Calvani, M. Searching for the Physical Drivers of the Eigenvector 1 Correlation Space. *ApJ* **558**, 553–560 (2001). astro-ph/0105343.
22. Miniutti, G., Fabian, A. C., Brandt, W. N., Gallo, L. C. & Boller, T. PHL 1092 as a transient extreme X-ray weak quasar. *MNRAS* **396**, L85–L89 (2009). 0904.3194.

23. Marinello, M., Rodríguez-Ardila, A., Marziani, P., Sigut, A. & Pradhan, A. Panchromatic properties of the extreme Fe II emitter PHL 1092. MNRAS **494**, 4187–4202 (2020). 2004.01811.
24. Panda, S. & Marziani, P. High Eddington quasars as discovery tools: current state and challenges. Frontiers in Astronomy and Space Sciences **10**, 1130103 (2023). 2210.15041.
25. Marziani, P. et al. Super-Eddington Accretion in Quasars. Universe **11**, 69 (2025). 2502.14713.
26. Shen, Y. & Ho, L. C. The diversity of quasars unified by accretion and orientation. Nature **513**, 210–213 (2014). 1409.2887.
27. Plotkin, R. M. et al. Multiwavelength Observations of Radio-quiet Quasars with Weak Emission Lines. ApJ **721**, 562–575 (2010). 1007.5058.
28. Wang, J.-M., Qiu, J., Du, P. & Ho, L. C. Self-shadowing Effects of Slim Accretion Disks in Active Galactic Nuclei: The Diverse Appearance of the Broad-line Region. ApJ **797**, 65 (2014). 1410.5285.
29. Netzer, H. The Physics and Evolution of Active Galactic Nuclei (2013).
30. Shakura, N. I. & Sunyaev, R. A. Black holes in binary systems. Observational appearance. A&A **24**, 337–355 (1973).
31. Wang, J.-M. & Zhou, Y.-Y. Self-similar Solution of Optically Thick Advection-dominated Flows. ApJ **516**, 420–424 (1999).
32. Du, P. et al. Supermassive Black Holes with High Accretion Rates in Active Galactic Nuclei. V. A New Size-Luminosity Scaling Relation for the Broad-line Region. ApJ **825**, 126 (2016). 1604.06218.

33. Du, P. et al. The Fundamental Plane of the Broad-line Region in Active Galactic Nuclei. ApJ **818**, L14 (2016). 1601.01391.
34. Cackett, E. M., Bentz, M. C. & Kara, E. Reverberation mapping of active galactic nuclei: from X-ray corona to dusty torus. iScience **24**, 102557 (2021). 2105.06926.
35. Kammoun, E. S., Dovčiak, M., Papadakis, I. E., Caballero-García, M. D. & Karas, V. UV/Optical Disk Thermal Reverberation in Active Galactic Nuclei: An In-depth Study with an Analytic Prescription for Time-lag Spectra. ApJ **907**, 20 (2021). 2011.08563.
36. Cackett, E. M., Horne, K. & Winkler, H. Testing thermal reprocessing in active galactic nuclei accretion discs. MNRAS **380**, 669–682 (2007). 0706.1464.
37. Svensson, R. & Zdziarski, A. A. Black Hole Accretion Disks with Coronae. ApJ **436**, 599 (1994).
38. Collin, S., Abrassart, A., Czerny, B., Dumont, A. M. & Mouchet, M. Accretion and emission processes in AGN: the UV-X connection. In Rocca-Volmerange, B. & Sol, H. (eds.) EAS Publications Series, vol. 1 of EAS Publications Series, 35–51 (2001). astro-ph/0003108.
39. Secunda, A., Jiang, Y.-F. & Greene, J. E. Simulating X-Ray Reverberation in the Ultraviolet-emitting Regions of Active Galactic Nuclei Accretion Disks with Three-dimensional Multifrequency Radiation Magnetohydrodynamic Simulations. ApJ **965**, L29 (2024). 2311.10820.
40. Secunda, A., Jiang, Y.-F. & Greene, J. E. Continuum Reverberation in Active Galactic Nuclei Disks Only with Sufficient X-Ray Luminosity and Low Albedo. ApJ **984**, 19 (2025). 2501.06304.
41. Wang, J.-M., Liu, J.-R., Ho, L. C. & Du, P. Accretion-modified Stars in Accretion Disks of Active Galactic Nuclei: Slowly Transient Appearance. ApJ **911**, L14 (2021). 2103.07708.

42. Tagawa, H., Kimura, S. S., Haiman, Z., Perna, R. & Bartos, I. Observable Signatures of Stellar-mass Black Holes in Active Galactic Nuclei. ApJ **946**, L3 (2023). 2303.02172.
43. Woosley, S. E., Heger, A. & Weaver, T. A. The evolution and explosion of massive stars. Reviews of Modern Physics **74**, 1015–1071 (2002).
44. Graham, M. J. et al. Candidate Electromagnetic Counterpart to the Binary Black Hole Merger Gravitational-Wave Event S190521g*. Phys. Rev. Lett. **124**, 251102 (2020). 2006.14122.
45. Graham, M. J. et al. A Light in the Dark: Searching for Electromagnetic Counterparts to Black Hole-Black Hole Mergers in LIGO/Virgo O3 with the Zwicky Transient Facility. ApJ **942**, 99 (2023). 2209.13004.
46. He, L. et al. A Systematic Search for AGN Flares in ZTF Data Release 23. arXiv e-prints arXiv:2507.20232 (2025). 2507.20232.
47. Abbott, R. et al. GW190521: A Binary Black Hole Merger with a Total Mass of $150 M_{\odot}$. Phys. Rev. Lett. **125**, 101102 (2020). 2009.01075.
48. The LIGO Scientific Collaboration, the Virgo Collaboration & the KAGRA Collaboration. GW231123: a Binary Black Hole Merger with Total Mass $190 - 265 M_{\odot}$. arXiv e-prints arXiv:2507.08219 (2025). 2507.08219.
49. Samsing, J. et al. AGN as potential factories for eccentric black hole mergers. Nature **603**, 237–240 (2022). 2010.09765.
50. Yang, J. et al. The nearby extreme accretion and feedback system PDS 456: finding a complex radio-emitting nucleus. MNRAS **500**, 2620–2626 (2021). 2008.05194.
51. Mapelli, M., Bouffanais, Y., Santoliquido, F., Arca Sedda, M. & Artale, M. C. The cosmic evolution of binary black holes in young, globular, and nuclear star clusters: rates, masses, spins, and mixing fractions. MNRAS **511**, 5797–5816 (2022). 2109.06222.

52. Vaccaro, M. P. Hierarchical Black Hole Mergers in AGN Disks: Tracing Massive Black Hole Growth Across Cosmic Time. arXiv e-prints arXiv:2508.15337 (2025). 2508.15337.
53. Masterson, M. et al. Millihertz oscillations near the innermost orbit of a supermassive black hole. Nature **638**, 370–375 (2025). 2501.01581.
54. Miniutti, G. et al. Nine-hour X-ray quasi-periodic eruptions from a low-mass black hole galactic nucleus. Nature **573**, 381–384 (2019). 1909.04693.
55. Giustini, M., Miniutti, G. & Saxton, R. D. X-ray quasi-periodic eruptions from the galactic nucleus of RX J1301.9+2747. A&A **636**, L2 (2020). 2002.08967.
56. Arcodia, R. et al. X-ray quasi-periodic eruptions from two previously quiescent galaxies. Nature **592**, 704–707 (2021). 2104.13388.
57. Chakraborty, J. et al. Possible X-Ray Quasi-periodic Eruptions in a Tidal Disruption Event Candidate. ApJ **921**, L40 (2021). 2110.10786.
58. Arcodia, R. et al. The more the merrier: SRG/eROSITA discovers two further galaxies showing X-ray quasi-periodic eruptions. A&A **684**, A64 (2024). 2401.17275.
59. Jiang, N. & Pan, Z. Embers of Active Galactic Nuclei: Tidal Disruption Events and Quasiperiodic Eruptions. ApJ **983**, L18 (2025). 2503.17609.
60. Bourdarot, G. & Eisenhauer, F. Kilometer-baseline interferometry: science drivers for the next generation instrument. arXiv e-prints arXiv:2410.22063 (2024). 2410.22063.
61. Ruan, W.-H., Liu, C., Guo, Z.-K., Wu, Y.-L. & Cai, R.-G. The LISA-Taiji network. Nature Astronomy **4**, 108–109 (2020). 2002.03603.
62. Vanden Berk, D. E. et al. Composite Quasar Spectra from the Sloan Digital Sky Survey. AJ **122**, 549–564 (2001). astro-ph/0105231.

63. Krawczyk, C. M. et al. Mean Spectral Energy Distributions and Bolometric Corrections for Luminous Quasars. ApJS **206**, 4 (2013). 1304.5573.
64. Du, P. et al. Supermassive Black Holes with High Accretion Rates in Active Galactic Nuclei. IX. 10 New Observations of Reverberation Mapping and Shortened $H\beta$ Lags. ApJ **856**, 6 (2018). 1802.03022.
65. U, V. et al. The Lick AGN Monitoring Project 2016: Velocity-resolved $H\beta$ Lags in Luminous Seyfert Galaxies. ApJ **925**, 52 (2022). 2111.14849.
66. Hu, C. et al. Supermassive Black Holes with High Accretion Rates in Active Galactic Nuclei. XII. Reverberation Mapping Results for 15 PG Quasars from a Long-duration High-cadence Campaign. ApJS **253**, 20 (2021).
67. Hu, C. et al. Supermassive Black Holes with High Accretion Rates in Active Galactic Nuclei. XIV. Long-duration High-cadence Reverberation Mapping Results for 11 PG Quasars. ApJS **278**, 61 (2025). 2505.01993.
68. Woo, J.-H. et al. The Seoul National University AGN Monitoring Project. III. $H\beta$ Lag Measurements of 32 Luminous Active Galactic Nuclei and the High-luminosity End of the Size–Luminosity Relation. ApJ **962**, 67 (2024). 2311.15518.
69. Bao, D.-W. et al. Monitoring AGNs with $H\beta$ Asymmetry. III. Long-term Reverberation Mapping Results of 15 Palomar-Green Quasars. ApJS **262**, 14 (2022). 2207.00297.
70. Edelson, R. et al. X-Ray Spectral Variability and Rapid Variability of the Soft X-Ray Spectrum Seyfert 1 Galaxies Arakelian 564 and Ton S180. ApJ **568**, 610–626 (2002). astro-ph/0108387.
71. Mortlock, D. J. et al. A luminous quasar at a redshift of $z = 7.085$. Nature **474**, 616–619 (2011). 1106.6088.

72. Bañados, E. et al. An 800-million-solar-mass black hole in a significantly neutral Universe at a redshift of 7.5. Nature **553**, 473–476 (2018). 1712.01860.
73. GRAVITY Collaboration et al. The size-luminosity relation of local active galactic nuclei from interferometric observations of the broad-line region. A&A **684**, A167 (2024). 2401.07676.
74. Du, P. et al. Supermassive Black Holes with High Accretion Rates in Active Galactic Nuclei. IV. $H\beta$ Time Lags and Implications for Super-Eddington Accretion. ApJ **806**, 22 (2015). 1504.01844.
75. Hu, C. et al. Supermassive Black Holes with High Accretion Rates in Active Galactic Nuclei. XII. Reverberation Mapping Results for 15 PG Quasars from a Long-duration High-cadence Campaign. ApJS **253**, 20 (2021).
76. Peterson, B. M. et al. On Uncertainties in Cross-Correlation Lags and the Reality of Wavelength-dependent Continuum Lags in Active Galactic Nuclei. PASP **110**, 660–670 (1998). astro-ph/9802103.
77. Denney, K. D. et al. Reverberation Mapping Measurements of Black Hole Masses in Six Local Seyfert Galaxies. ApJ **721**, 715–737 (2010). 1006.4160.
78. Grier, C. J. et al. Reverberation Mapping Results for Five Seyfert 1 Galaxies. ApJ **755**, 60 (2012). 1206.6523.
79. Fausnaugh, M. M. et al. Reverberation Mapping of Optical Emission Lines in Five Active Galaxies. ApJ **840**, 97 (2017). 1610.00008.
80. Bentz, M. C. et al. The Lick AGN Monitoring Project: Broad-line Region Radii and Black Hole Masses from Reverberation Mapping of $H\beta$. ApJ **705**, 199–217 (2009). 0908.0003.
81. Barth, A. J. et al. The Lick AGN Monitoring Project 2011: Spectroscopic Campaign and Emission-line Light Curves. ApJS **217**, 26 (2015). 1503.01146.

82. Zastrocky, T. E. et al. Monitoring AGNs with $H\beta$ Asymmetry. IV. First Reverberation Mapping Results of 14 Active Galactic Nuclei. ApJS **272**, 29 (2024). 2404.07343.
83. Malik, U. et al. OzDES Reverberation Mapping Program: $H\beta$ lags from the 6-yr survey. MNRAS **520**, 2009–2023 (2023). 2210.03977.
84. Shen, Y. et al. The Sloan Digital Sky Survey Reverberation Mapping Project: Key Results. ApJS **272**, 26 (2024). 2305.01014.
85. Flesch, E. W. The Million Quasars (Milliquas) Catalogue, v8. The Open Journal of Astrophysics **6**, 49 (2023). 2308.01505.
86. Nakoneczny, S. J. et al. QZO: A Catalog of 5 Million Quasars from the Zwicky Transient Facility. arXiv e-prints arXiv:2502.13054 (2025). 2502.13054.
87. Lu, K.-X. et al. Supermassive Black Hole and Broad-line Region in NGC 5548: Results from Five-season Reverberation Mapping. ApJS **263**, 10 (2022). 2209.10853.
88. Minezaki, T. et al. Reverberation Measurements of the Inner Radii of the Dust Tori in Quasars. ApJ **886**, 150 (2019). 1910.08722.
89. Begelman, M. C., Frank, J. & Shlosman, I. Accretion Disks and the Link Between an AGN and its Host Galaxy. In Meyer, F. (ed.) Theory of Accretion Disks, vol. 290 of NATO Advanced Study Institute (ASI) Series C, 373 (1989).
90. Wang, J.-M. et al. Tidally disrupted dusty clumps as the origin of broad emission lines in active galactic nuclei. Nature Astronomy **1**, 775–783 (2017). 1710.03419.
91. Zhou, H. et al. Fast inflows as the adjacent fuel of supermassive black hole accretion disks in quasars. Nature **573**, 83–86 (2019).
92. Laor, A. & Netzer, H. Massive thin accretion discs. - I. Calculated spectra. MNRAS **238**, 897–916 (1989).

93. Boroson, T. A. & Green, R. F. The Emission-Line Properties of Low-Redshift Quasi-stellar Objects. ApJS **80**, 109 (1992).
94. Yang, S., Du, P. & Wang, J.-M. Dependence of Virial Factors on Optical Spectral Properties of Active Galactic Nuclei. ApJS **274**, 24 (2024). 2407.04257.
95. Pei, L. et al. Space Telescope and Optical Reverberation Mapping Project. V. Optical Spectroscopic Campaign and Emission-line Analysis for NGC 5548. ApJ **837**, 131 (2017). 1702.01177.
96. Homayouni, Y. et al. AGN STORM 2. V. Anomalous Behavior of the C IV Light Curve of Mrk 817. ApJ **963**, 123 (2024). 2308.00742.
97. Peterson, B. M. et al. Reverberation Mapping of the Seyfert 1 Galaxy NGC 7469. ApJ **795**, 149 (2014). 1409.4448.
98. Lu, K.-X. et al. A correction method for the telluric absorptions and application to Lijiang Observatory. Research in Astronomy and Astrophysics **21**, 183 (2021). 2103.08136.
99. Peterson, B. M. et al. Central Masses and Broad-Line Region Sizes of Active Galactic Nuclei. II. A Homogeneous Analysis of a Large Reverberation-Mapping Database. ApJ **613**, 682–699 (2004). astro-ph/0407299.
100. Rodríguez-Pascual, P. M. et al. Steps toward Determination of the Size and Structure of the Broad-Line Region in Active Galactic Nuclei. IX. Ultraviolet Observations of Fairall 9. ApJS **110**, 9–20 (1997).
101. Hu, C. et al. Supermassive Black Holes with High Accretion Rates in Active Galactic Nuclei. III. Detection of Fe II Reverberation in Nine Narrow-line Seyfert 1 Galaxies. ApJ **804**, 138 (2015). 1503.03611.
102. Barth, A. J. et al. The Lick AGN Monitoring Project 2011: Fe II Reverberation from the Outer Broad-line Region. ApJ **769**, 128 (2013). 1304.4643.

103. Guo, H., Barth, A. J. & Wang, S. Active Galactic Nuclei Continuum Reverberation Mapping Based on Zwicky Transient Facility Light Curves. ApJ **940**, 20 (2022). 2207.06432.
104. Netzer, H. Continuum reverberation mapping and a new lag-luminosity relationship for AGN. MNRAS **509**, 2637–2646 (2022). 2110.05512.
105. Korista, K. T. & Goad, M. R. Quantifying the impact of variable BLR diffuse continuum contributions on measured continuum interband delays. MNRAS **489**, 5284–5300 (2019). 1908.07757.
106. Gaskell, C. M. & Peterson, B. M. The Accuracy of Cross-Correlation Estimates of Quasar Emission-Line Region Sizes. ApJS **65**, 1 (1987).
107. Jiang, Y.-F. et al. Detection of Time Lags between Quasar Continuum Emission Bands Based On Pan-STARRS Light Curves. ApJ **836**, 186 (2017). 1612.08747.
108. Grier, C. J. et al. The Sloan Digital Sky Survey Reverberation Mapping Project: $H\alpha$ and $H\beta$ Reverberation Measurements from First-year Spectroscopy and Photometry. ApJ **851**, 21 (2017). 1711.03114.
109. Zu, Y., Kochanek, C. S. & Peterson, B. M. An Alternative Approach to Measuring Reverberation Lags in Active Galactic Nuclei. ApJ **735**, 80 (2011). 1008.0641.
110. Li, Y.-R., Wang, J.-M. & Bai, J.-M. A Non-parametric Approach to Constrain the Transfer Function in Reverberation Mapping. ApJ **831**, 206 (2016). 1608.03741.
111. Shen, Y. et al. The Sloan Digital Sky Survey Reverberation Mapping Project: Technical Overview. ApJS **216**, 4 (2015). 1408.5970.
112. Grier, C. J. et al. The Structure of the Broad-line Region in Active Galactic Nuclei. I. Reconstructed Velocity-delay Maps. ApJ **764**, 47 (2013). 1210.2397.
113. Lynden-Bell, D. Galactic Nuclei as Collapsed Old Quasars. Nature **223**, 690–694 (1969).

114. Blandford, R. D., Netzer, H., Woltjer, L., Courvoisier, T. J. L. & Mayor, M. (eds.). Active Galactic Nuclei (1990).
115. Pancoast, A., Brewer, B. J. & Treu, T. Geometric and Dynamical Models of Reverberation Mapping Data. ApJ **730**, 139 (2011). 1101.4952.
116. Li, Y.-R. et al. Supermassive Black Holes with High Accretion Rates in Active Galactic Nuclei. VIII. Structure of the Broad-line Region and Mass of the Central Black Hole in Mrk 142. ApJ **869**, 137 (2018). 1811.06302.
117. Gravity Collaboration et al. Spatially resolved rotation of the broad-line region of a quasar at sub-parsec scale. Nature **563**, 657–660 (2018). 1811.11195.
118. Wang, J.-M., Songsheng, Y.-Y., Li, Y.-R., Du, P. & Zhang, Z.-X. A parallax distance to 3C 273 through spectroastrometry and reverberation mapping. Nature Astronomy **4**, 517–525 (2020). 1906.08417.
119. Chen, Y.-X. & Lin, D. N. C. The Population of Massive Stars in Active Galactic Nuclei Disks. ApJ **967**, 88 (2024). 2404.08780.
120. Wang, J.-M. et al. Star Formation in Self-gravitating Disks in Active Galactic Nuclei. III. Efficient Production of Iron and Infrared Spectral Energy Distributions. ApJ **954**, 84 (2023). 2311.06782.
121. Verner, E. et al. Fe II Diagnostic Tools for Quasars. ApJ **611**, 780–785 (2004). astro-ph/0404593.
122. Verner, E., Bruhweiler, F., Johansson, S. & Peterson, B. Fe ii emission spectra in AGN: observations and theoretical interpretation. Physica Scripta Volume T **134**, 014006 (2009).
123. Netzer, H. & Trakhtenbrot, B. Cosmic Evolution of Mass Accretion Rate and Metallicity in Active Galactic Nuclei. ApJ **654**, 754–763 (2007). astro-ph/0607654.

124. Rauch, K. P. & Blandford, R. D. Microlensing and the Structure of Active Galactic Nucleus Accretion Disks. ApJ **381**, L39 (1991).
125. Morgan, C. W., Kochanek, C. S., Morgan, N. D. & Falco, E. E. The Quasar Accretion Disk Size-Black Hole Mass Relation. ApJ **712**, 1129–1136 (2010). 1002.4160.
126. Cornachione, M. A. et al. A Microlensing Accretion Disk Size Measurement in the Lensed Quasar WFI 2026-4536. ApJ **895**, 125 (2020). 1911.06218.
127. Pan, X. et al. Mrk 1239: a Type-2 Counterpart of Narrow-line Seyfert-1? ApJ **912**, 118 (2021). 2105.13672.
128. Li, Y.-R. et al. Spectroastrometry and Reverberation Mapping of Active Galactic Nuclei. II. Measuring Geometric Distances and Black Hole Masses of Four Nearby Quasars. ApJ **988**, 42 (2025). 2502.18856.
129. Kang, W.-Y. et al. A Surprising Excess of Radio Emission in Extremely Stable Quasars: A Unique Clue to Jet Launching? ApJ **971**, 60 (2024). 2406.13169.
130. Artymowicz, P., Lin, D. N. C. & Wampler, E. J. Star Trapping and Metallicity Enrichment in Quasars and Active Galactic Nuclei. ApJ **409**, 592 (1993).
131. Wang, J.-M. et al. Star Formation in Self-gravitating Disks in Active Galactic Nuclei. I. Metallicity Gradients in Broad-line Regions. ApJ **739**, 3 (2011). 1107.3620.
132. Wang, J.-M. et al. Star Formation in Self-gravitating Disks in Active Galactic Nuclei. II. Episodic Formation of Broad-line Regions. ApJ **746**, 137 (2012). 1202.0062.
133. Fan, X. & Wu, Q. In Situ Star Formation in Accretion Disks and Explanation of Correlation between the Black Hole Mass and Metallicity in Active Galactic Nuclei. ApJ **944**, 159 (2023). 2212.06363.

134. Cantiello, M., Jermyn, A. S. & Lin, D. N. C. Stellar Evolution in AGN Disks. ApJ **910**, 94 (2021). 2009.03936.
135. Kato, S., Fukue, J. & Mineshige, S. Black-Hole Accretion Disks – Towards a New Paradigm – (2008).
136. Ingram, A. R. & Motta, S. E. A review of quasi-periodic oscillations from black hole X-ray binaries: Observation and theory. New A Rev. **85**, 101524 (2019). 2001.08758.
137. Gierliński, M., Middleton, M., Ward, M. & Done, C. A periodicity of ~ 1 hour in X-ray emission from the active galaxy RE J1034+396. Nature **455**, 369–371 (2008).
138. Lu, K.-X. et al. Supermassive Black Holes with High Accretion Rates in Active Galactic Nuclei. X. Optical Variability Characteristics. ApJ **877**, 23 (2019). 1904.03393.
139. Lewin, C. et al. AGN STORM 2. VII. A Frequency-resolved Map of the Accretion Disk in Mrk 817: Simultaneous X-Ray Reverberation and UVOIR Disk Reprocessing Time Lags. ApJ **974**, 271 (2024). 2409.09115.
140. Wang, Y.-L., Liu, J.-R. & Wang, J.-M. Continuum reverberation mapping of accretion disks depending on the vertical structures in active galactic nuclei. A&A **695**, A143 (2025).
141. Kara, E. et al. UV-Optical Disk Reverberation Lags despite a Faint X-Ray Corona in the Active Galactic Nucleus Mrk 335. ApJ **947**, 62 (2023). 2302.07342.
142. Wang, J.-M., Liu, J.-R., Ho, L. C., Li, Y.-R. & Du, P. Accretion-modified Stars in Accretion Disks of Active Galactic Nuclei: Gravitational-wave Bursts and Electromagnetic Counterparts from Merging Stellar Black Hole Binaries. ApJ **916**, L17 (2021). 2106.07334.
143. Secunda, A. et al. Orbital Migration of Interacting Stellar Mass Black Holes in Disks around Supermassive Black Holes. ApJ **878**, 85 (2019). 1807.02859.

144. Secunda, A. et al. Orbital Migration of Interacting Stellar Mass Black Holes in Disks around Supermassive Black Holes. II. Spins and Incoming Objects. ApJ **903**, 133 (2020). 2004. 11936.
145. Wang, M., Ma, Y. & Wu, Q. Accretion-modified stellar-mass black hole distribution and milli-Hz gravitational wave backgrounds from galaxy centre. MNRAS **520**, 4502–4516 (2023). 2212.05724.
146. Yang, Y. et al. Hierarchical Black Hole Mergers in Active Galactic Nuclei. Phys. Rev. Lett. **123**, 181101 (2019). 1906.09281.
147. Liu, J.-R., Wang, Y.-L. & Wang, J.-M. Accretion-modified Stars in Accretion Disks of Active Galactic Nuclei: Observational Characteristics in Different Regions of the Disks. ApJ **969**, 37 (2024). 2405.02855.
148. Komossa, S. & Grupe, D. The Extremes of Continuum and Emission-Line Variability of AGN: Changing-Look Events and Binary SMBHS. Serbian Astronomical Journal **209**, 1–24 (2024).
149. Wang, J.-M. & Bon, E. Changing-look active galactic nuclei: close binaries of supermassive black holes in action. A&A **643**, L9 (2020). 2010.04417.
150. Guo, W.-J. et al. Changing-look Active Galactic Nuclei from the Dark Energy Spectroscopic Instrument. II. Statistical Properties from the First Data Release. ApJS **278**, 28 (2025). 2408.00402.
151. Reardon, D. J. et al. Search for an Isotropic Gravitational-wave Background with the Parkes Pulsar Timing Array. ApJ **951**, L6 (2023). 2306.16215.
152. EPTA Collaboration et al. The second data release from the European Pulsar Timing Array. III. Search for gravitational wave signals. A&A **678**, A50 (2023). 2306.16214.

153. Xu, H. et al. Searching for the Nano-Hertz Stochastic Gravitational Wave Background with the Chinese Pulsar Timing Array Data Release I. Research in Astronomy and Astrophysics **23**, 075024 (2023). 2306.16216.
154. Wang, J.-M., Songsheng, Y.-Y., Li, Y.-R. & Yu, Z. Kinematic Signatures of Reverberation Mapping of Close Binaries of Supermassive Black Holes in Active Galactic Nuclei. ApJ **862**, 171 (2018). 1806.06487.
155. Du, P. et al. Monitoring AGNs with H β Asymmetry. I. First Results: Velocity-resolved Reverberation Mapping. ApJ **869**, 142 (2018). 1810.11996.
156. Songsheng, Y.-Y., Xiao, M., Wang, J.-M. & Ho, L. C. Kinematic Signatures of Reverberation Mapping of Close Binaries of Supermassive Black Holes in Active Galactic Nuclei. II. Atlas of Two-dimensional Transfer Functions. ApJS **247**, 3 (2020). 1912.12965.
157. Fu, Y.-X. et al. Continuum Reverberation Mapping of Accretion Disks Surrounding Supermassive Black Hole Binaries: Observational Signatures. MNRAS (2025). 2507.21671.
158. Songsheng, Y.-Y., Wang, J.-M. & Li, Y.-R. The VLT Interferometric Measurements of Active Galactic Nuclei: Effects of Angular Momentum Distributions of Clouds in the Broad-line Region. ApJ **883**, 184 (2019).
159. Songsheng, Y.-Y. & Wang, J.-M. Differential Interferometric Signatures of Close Binaries of Supermassive Black Holes in Active Galactic Nuclei. II. Merged Broad-line Regions. ApJ **945**, 89 (2023). 2302.08338.
160. Chiang, J. & Murray, N. Reverberation Mapping and the Disk-Wind Model of the Broad-Line Region. ApJ **466**, 704 (1996). astro-ph/9511006.
161. Frank, J., King, A. & Raine, D. J. Accretion Power in Astrophysics: Third Edition (2002).
162. Abramowicz, M. A., Czerny, B., Lasota, J. P. & Szuszkiewicz, E. Slim Accretion Disks. ApJ **332**, 646 (1988).

163. Liu, H., Jiang, Y.-F., Quataert, E., Greene, J. E. & Ma, Y. The Balmer Break and Optical Continuum of Little Red Dots From Super-Eddington Accretion. [arXiv e-prints](#) arXiv:2507.07190 (2025). 2507.07190.
164. Du, P. [et al.](#) Supermassive Black Holes with High Accretion Rates in Active Galactic Nuclei. VI. Velocity-resolved Reverberation Mapping of the H β Line. [ApJ](#) **820**, 27 (2016). 1602.01922.
165. Chen, Y.-X., Jiang, Y.-F. & Goodman, J. Accretion of Active Galactic Nucleus Stars Under the Influence of Disk Geometry. [ApJ](#) **987**, 188 (2025). 2505.13951.
166. McKernan, B. [et al.](#) McFACTS I: Testing the LVK AGN channel with Monte Carlo For AGN Channel Testing & Simulation (McFACTS). [arXiv e-prints](#) arXiv:2410.16515 (2024). 2410.16515.
167. Yang, S.-C., Han, W.-B., Tagawa, H., Li, S. & Zhang, C. Indication for a Compact Object Next to a LIGO–Virgo Binary Black Hole Merger. [ApJ](#) **988**, L41 (2025). 2401.01743.

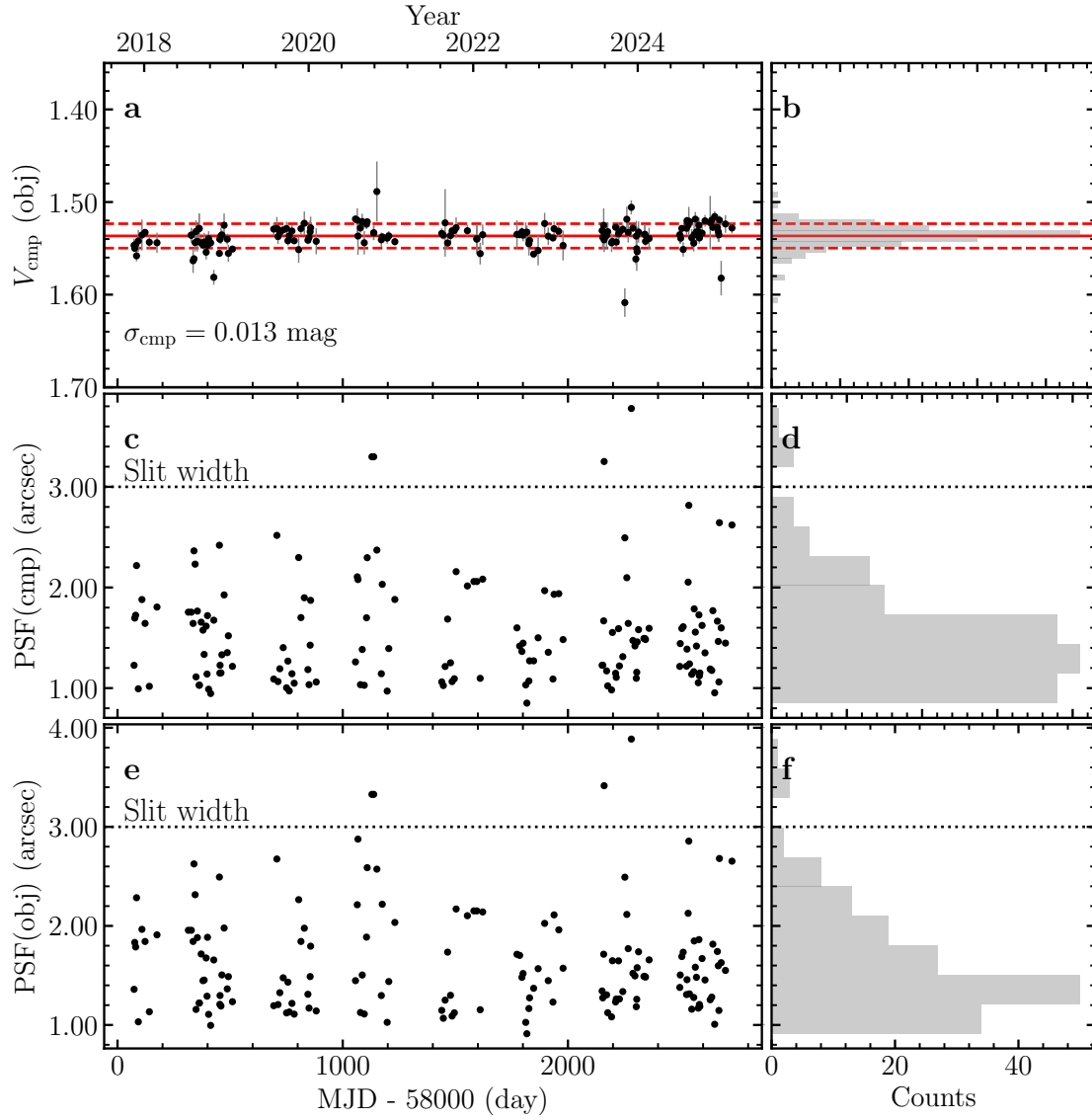


Figure 5: Panel **a**: V-band LC of the comparison star indicates that the star keeps constant with a very small scatter. Panel **c** and **e**: image PSF FWHMs of the comparison star and the target. We find $\text{FWHM}(\text{cmp}) \approx \text{FWHM}(\text{obj})$, showing that the host of PHL 1092 weakly contaminates the nuclear emissions. Panel **b**, **d**, **f** are distributions of the comparison star and seeing.

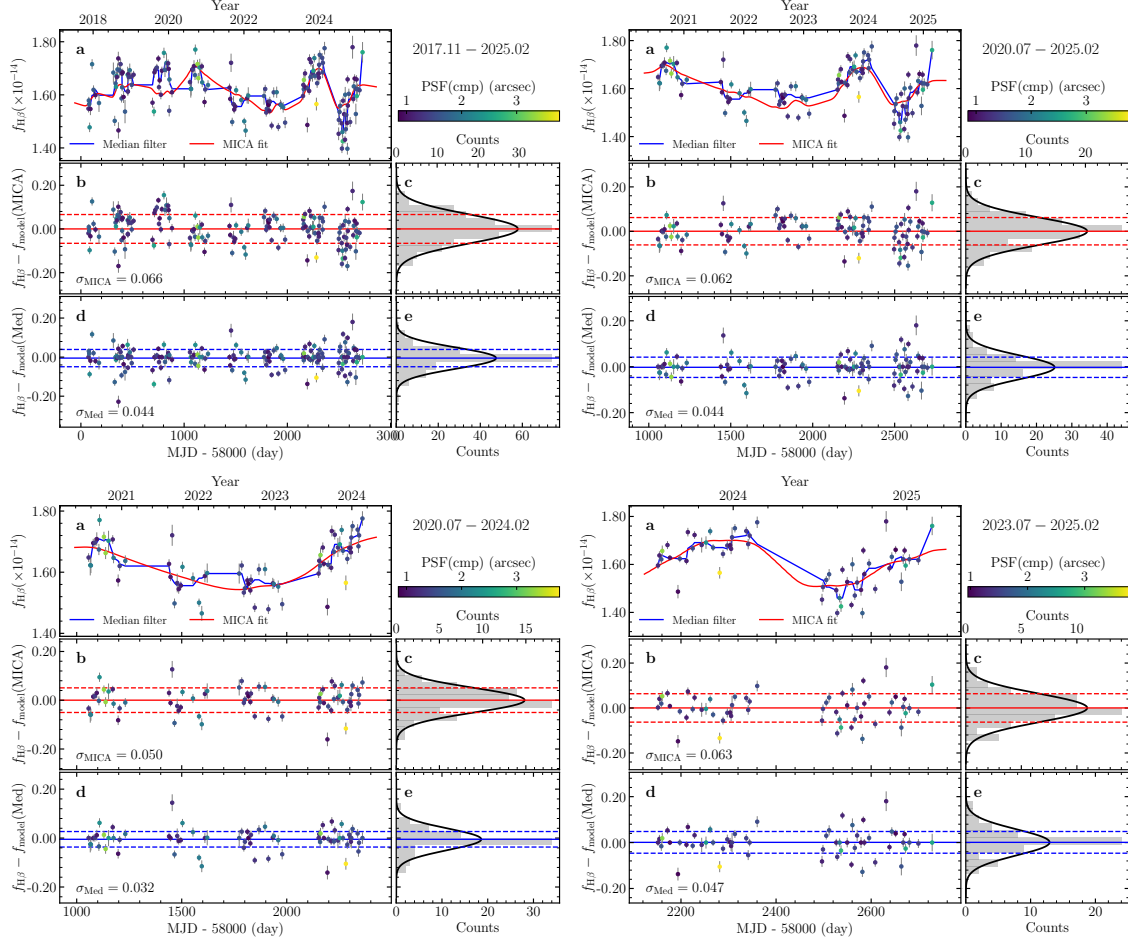


Figure 6: Panel **a** shows $H\beta$ LC with median-filter (blue) and MICA (red) model fits curves, colour-coded by the FWHM of the target’s image, which serves as a proxy for change of atmospheric seeing. Panels **d** and **c** present the residuals from the MICA and median-filter, respectively, with their corresponding residual distributions shown in panels **d** and **e**. Red/Blue solid and dashed lines in panels **b**, **d/c**, **e** mark the mean and standard deviations of residuals, respectively. In panels **b** and **c**, no correlation between seeing variations and residuals, indicating that the long-term variability is not caused by seeing changes. Solid black lines in panels **d** and **e** indicate Gaussian fits to the residual distributions, demonstrating the robustness of our results against aliasing effects.

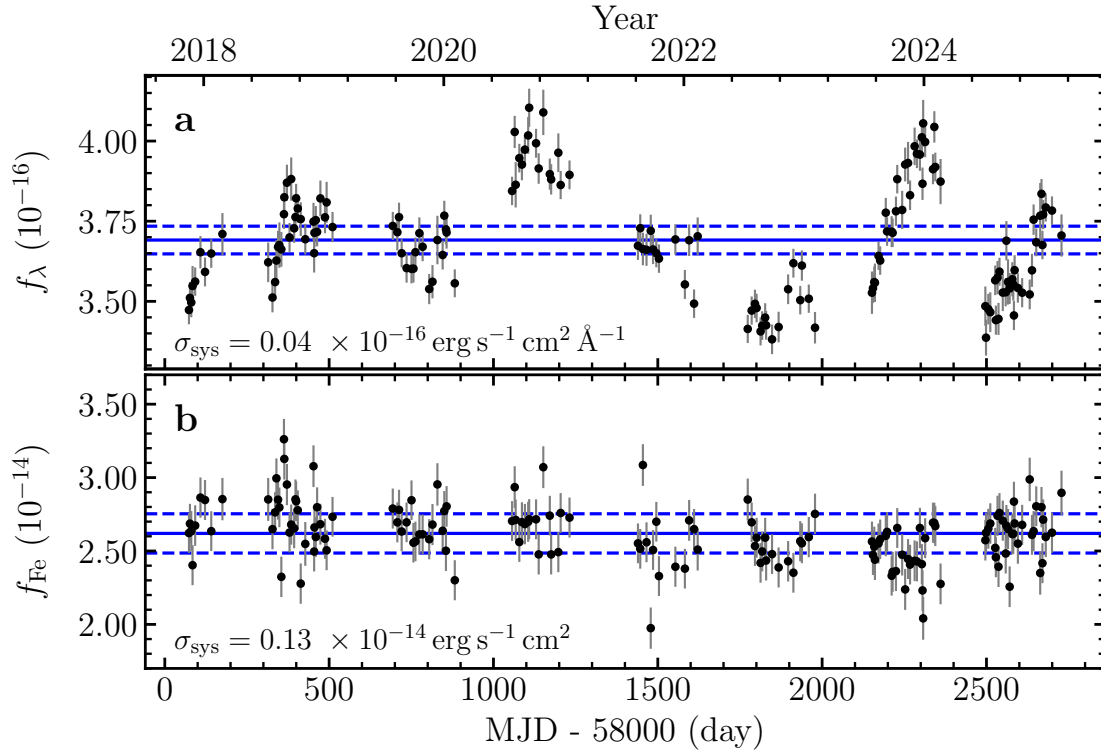


Figure 7: LCs of 5100 Å continuum (panel **a**) and integrated Fe II line (panel **b**), with the corresponding systematic uncertainties (σ_{sys}) included. Blue solid lines are the mean fluxes of 5100 Å continuum and Fe II line, while the dashed lines are the corresponding scatters, namely systematic uncertainties. No significant variation of the Fe II line is detected within $1 \sigma_{\text{sys}}$.

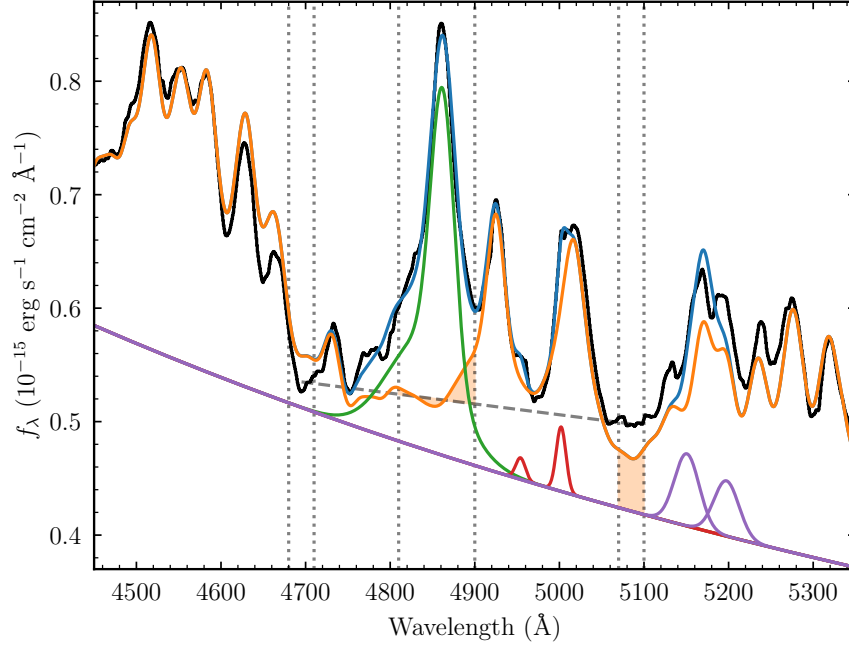


Figure 8: Possible Fe II residuals in the continuum and H β windows. The black line represents the mean spectrum from 2017 in the rest frame, while the blue line indicates the best-fit result. The orange line corresponds to the Fe II template from Ref.⁹³. The green line depicts the H β component, the red lines represent the [O III] emission lines, and the purple lines correspond to the coronal lines. Vertical dotted lines mark the positions of the H β line and the two continuum windows. The dashed lines indicate the continuum background determined by the integration method. The orange shaded area represents the possible Fe II contribution that may not be accounted for by the integration method within the measurement windows.

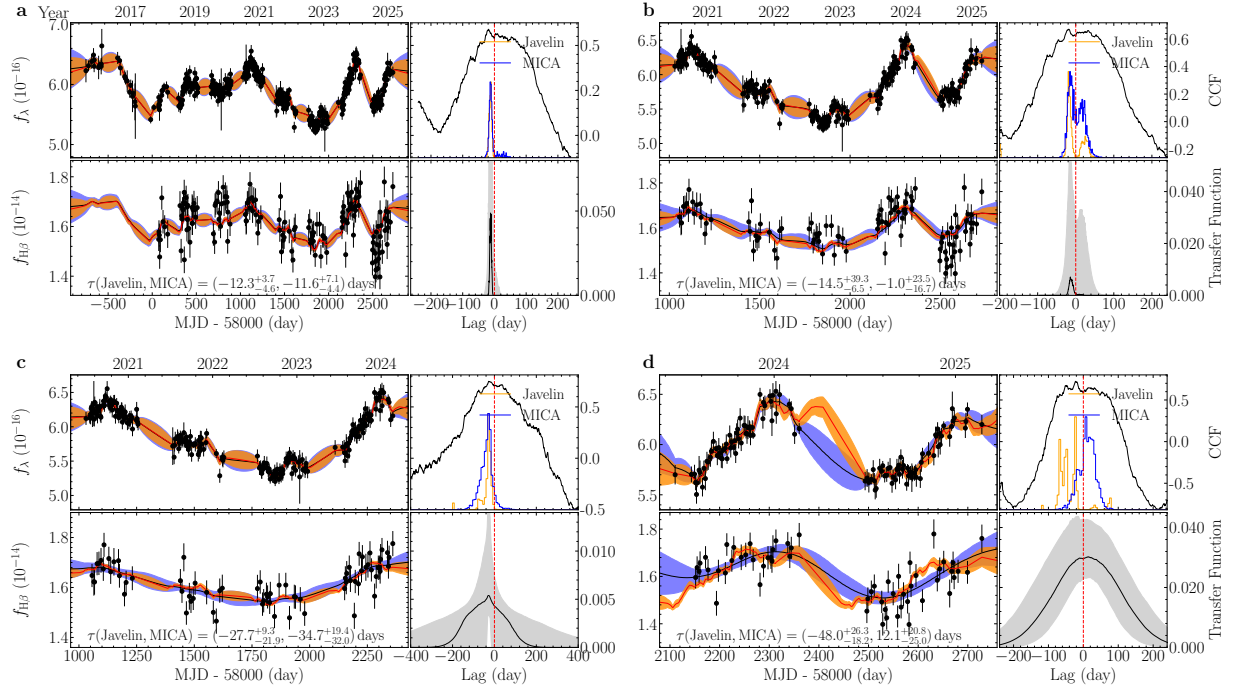


Figure 9: H β lags with respect to broad photometric LCs are determined for the four different periods. The results are consistent with those in Fig. 2. The photometric data are obtained with observations from CAHA-V, ZTF-r, and ATLAS-c. After performing intercalibration of the dataset, the LC is binned into two-day intervals.

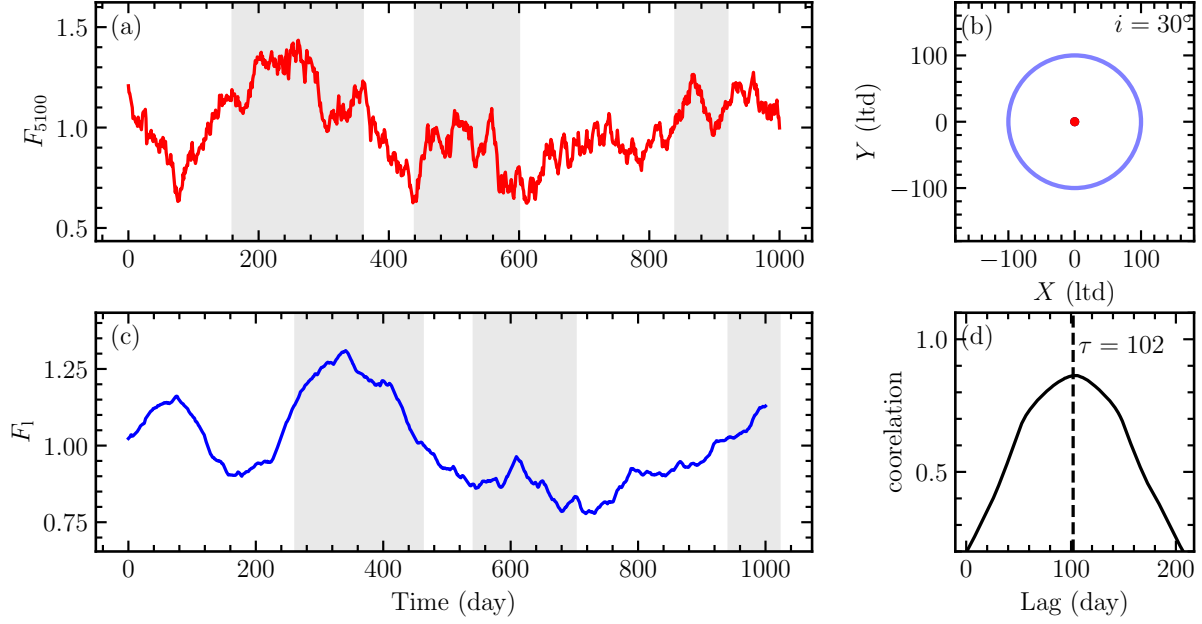


Figure 10: The 5100 Å and line LCs in the case of point source approximation (PSA). In such a case, X-ray, the ionizing photons and the 5100 Å share the same LCs. We take $R_{5100} = R_{\text{ion}} = R_X = 0$ and $R_{\text{BLR}} = R_{\text{H}\beta} = 100$ ltd in this simulation. (a) The 5100 Å LC; (b) The position of ionizing sources (red dots) and BLR clouds (blue ring). (c) The line LC; (d) The cross correlation between continuum at 5100 Å and line LC. The most features of the H β LC is that the extended BLRs smear variabilities with shorter timescales (than $R_{\text{H}\beta}/c$), but keep the large structures of the 5100 Å variations.

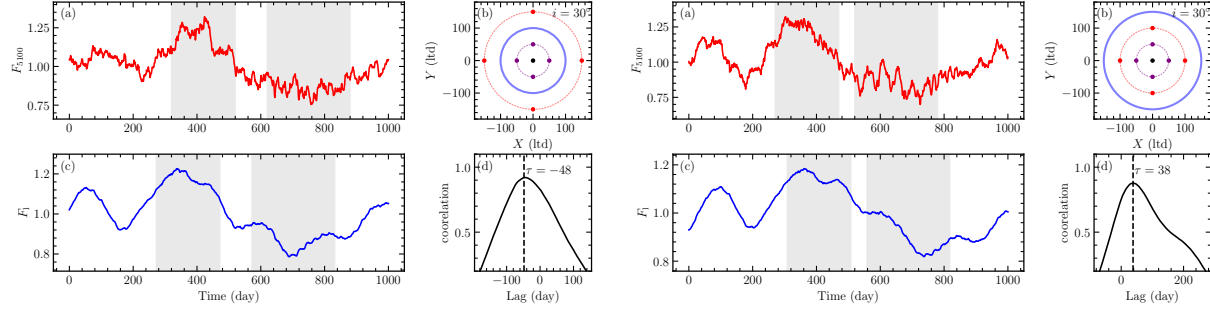


Figure 11: Left Panel: The 5100 Å and line LCs ionized by 4 uniformly distributed sources. The BLR is inside the 5100 Å sources. We take $(R_{\text{ion}}, R_{5100}, R_{H\beta}) = (50, 150, 100)$ ltd in the left panel. (a) the 5100 Å LC; (b) the position of X-ray source (black dots), ionizing sources (purple dots), BLR clouds (blue ring), and 5100 Å sources (red dots); (c) the line LC; (d) the cross correlation between the 5100 Å and line LCs. The LDRs appear in this case because of $R_{5100} > R_{H\beta}$. Right panel: we take $(R_{\text{ion}}, R_{5100}, R_{H\beta}) = (50, 100, 150)$ ltd, namely, the BLR is outside of the 5100 Å region ($R_{5100} < R_{H\beta}$), showing positive delays. The shadowed regions in two panel show the non-concordant reverberations with the 5100 Å. This is caused by the non-point source effects.

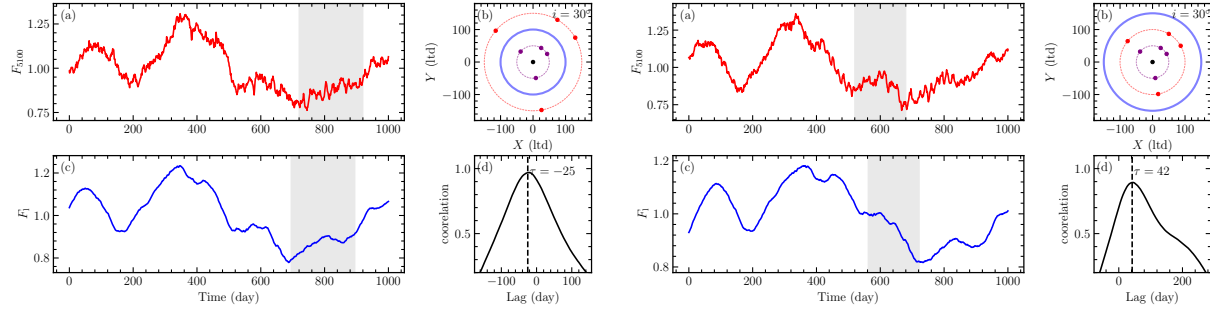


Figure 12: Left panel: The continuum and line LCs of a BLR ionized by 4 randomly distributed sources. The BLR is inside the 5100 region showing LRDs. We take $(R_{\text{ion}}, R_{5100}, R_{H\beta}) = (50, 150, 100)$ ltd in the left panel. Right panel: we take $(R_{\text{ion}}, R_{5100}, R_{H\beta}) = (50, 100, 150)$ ltd. The shadowed regions show non-concordant reverberations.

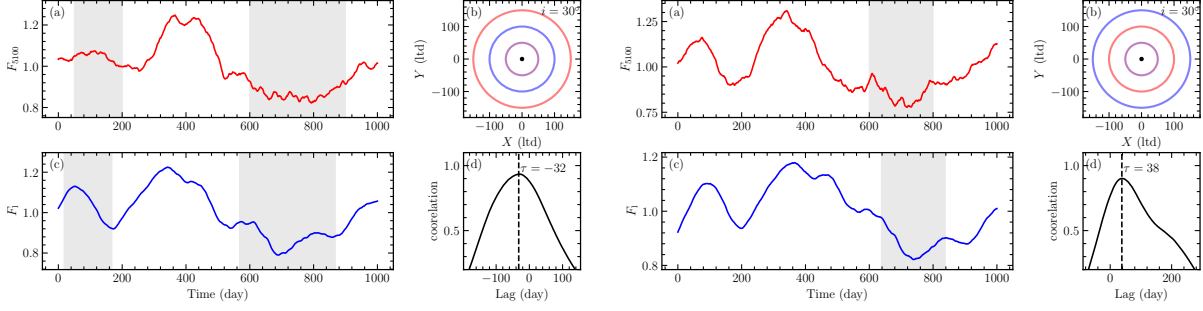


Figure 13: Left panel: The continuum and line LCs of a BLR ionized by a uniform ring of ionizing sources. The BLR is inside the 5100 Å region exhibiting the LDRs. We take $(R_{\text{ion}}, R_{5100}, R_{\text{H}\beta}) = (50, 150, 100)$ ltd in the left panel. Right panel: $(R_{\text{ion}}, R_{5100}, R_{\text{H}\beta}) = (50, 100, 150)$ ltd. The NPS effects are clear.

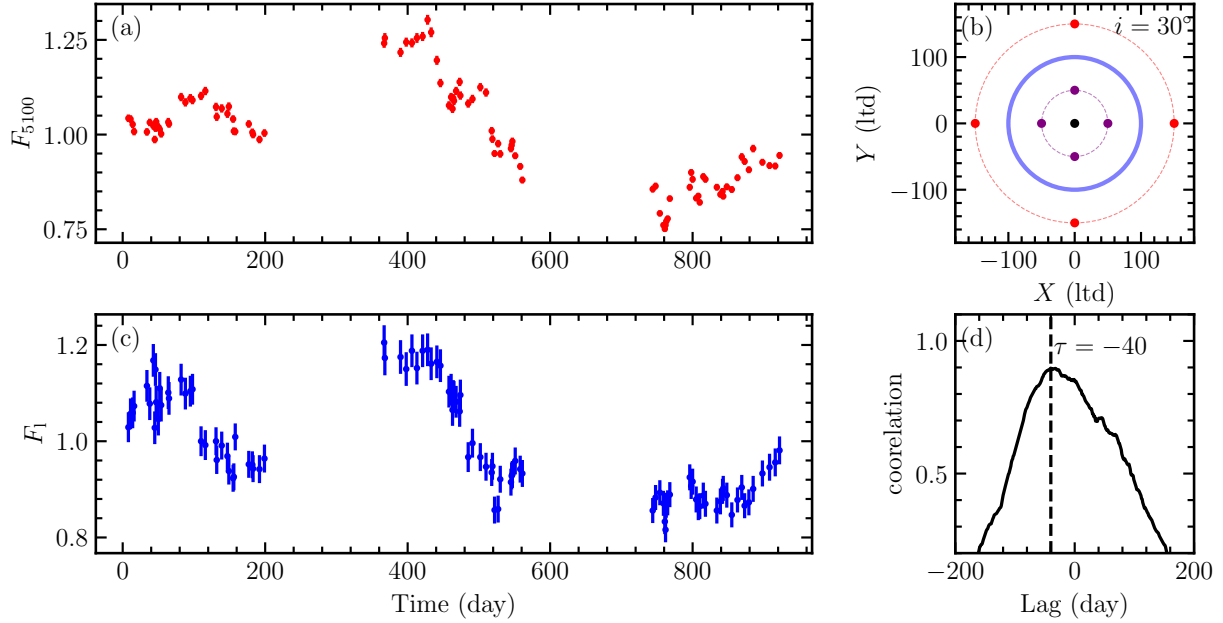


Figure 14: The same as Fig. 10, but the LC is sampled with a non-uniform cadence of 6 days and a season gap of 160 days. The relative uncertainties of continuum and line are 1% and 3%, respectively. The leading delays are consistent with that in Fig. 10, demonstrating the robustness of the present results from our eight-year campaign of PHL 1092.

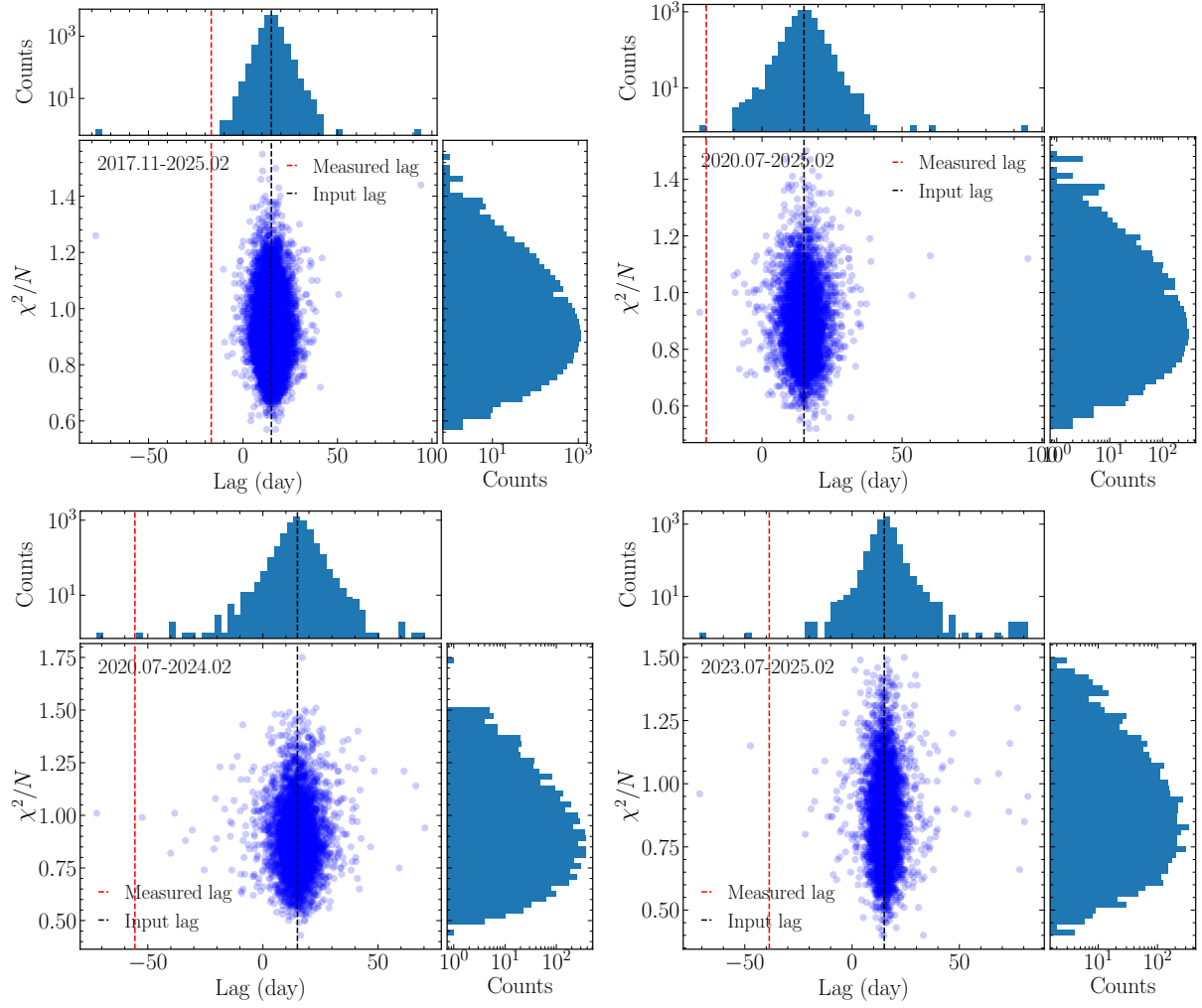


Figure 15: Distribution of $H\beta$ lags (MICA measured) from Monte Carlo simulations. The black dashed line indicates the input time lags of $\tau_{H\beta}^0 = 16$ days used to generate the mock LCs of $H\beta$ line, while the red dashed line shows the lag measured from the real data for different epochs.